

GEOMETRIC SINGULAR PERTURBATION ANALYSIS OF THE ACTIVE METABOLIC OSCILLATOR IN PANCREATIC β -CELLS

PRANNATH MOOLCHAND* AND MARTIN WECHSELBERGER†

Abstract. Pancreatic β -cells secrete insulin in response to blood sugar levels to maintain glucose homeostasis. This vital insulin exocytosis is controlled by the cell’s bursting behaviours, which are regulated by tight bidirectional coupling of inherent electrical and metabolic oscillators. The Integrated Oscillator Model suggests that slower metabolic oscillations are mediated either by glycolytic oscillations—through an independent active metabolic oscillator (AMO)—or by Ca^{2+} effects on ATP consumption via a passive metabolic oscillator (PMO). By clamping the Ca^{2+} and ATP dynamics, our study focuses on the decoupled AMO which is the driver of pulsatile dynamics. Using appropriate reference scales, we first non-dimensionalise the model to identify small parameters and processes evolving on different timescales. We show that the AMO can be recast as a surrogate relaxation oscillator, a more general class of multiple timescale problems involving oscillation cycles comprising fast and slow segments, which are amenable to rigorous analysis using the machinery of geometric singular perturbation theory. Using the parametrisation method to identify invariant manifolds and blow-up analysis to desingularise degenerate vector fields, we fully characterise the hierarchy of timescales and the complex singular geometry constituting the metabolic oscillations. Our work considerably extends the ‘fast-slow’ analysis of glycolytic oscillators and is a stepping stone towards understanding how the *slower* metabolic system temporally patterns the *faster* electrical bursting dynamics.

Key words. pancreatic beta-cell model, glycolytic oscillator, multiple timescales, geometric singular perturbation theory, parametrisation method, non-dimensionalisation, blow-up analysis

MSC codes. 34E13, 34E15, 34C26, 92C45

1 Introduction Insulin is the primary hormone regulating glucose uptake, and its secretion by pancreatic β -cells is fundamental to metabolic health, with dysfunction directly linked to diabetes [1]. β -cells share key electrophysiological traits with neurons, exhibiting excitability similar to the characteristic all-or-none response. Consequently, the modelling of β -cell dynamics has a rich history [1], evolving from the Chay-Keizer model [5], which itself descended from the biophysically grounded Hodgkin-Huxley formalism [11].

The architectural complexity of these models has grown in tandem with the discovery of diverse bursting regimes. Early ‘slow-fast’ singular perturbation models successfully captured *square-wave bursting* driven by the relatively rapid feedback of Ca^{2+} on membrane potential. However, these models fail to account for the much slower rhythms observed in islet studies, such as *compound bursting*—where clusters of bursts are separated by long silent periods—and *accordion bursting*, characterised by the rhythmic modulation of the burst plateau; see Figure 11 of [1]. Capturing these phenomena requires a multi-timescale architecture involving a third, even slower clock: a metabolic oscillator. This shift towards the pulsatile nature of insulin secretion [3] has led to models emphasising the bidirectional coupling between a fast electrical oscillator and a slower metabolic oscillator (see Figure 1).

While the fast electrical subsystem governs the immediate mechanics of exocytosis, the timing of the pulsatility is orchestrated by the slower metabolic subsystem. To investigate this interaction, Marinelli *et al.* [24, 23, 1] proposed the *Integrated Oscillator Model* (IOM); see subsections A.1 to A.3 for details of this 8D model. The

*School of Mathematics & Statistics, University of Sydney (prannath.moolchand@sydney.edu.au)

†School of Mathematics & Statistics, University of Sydney (martin.wechselberger@sydney.edu.au).

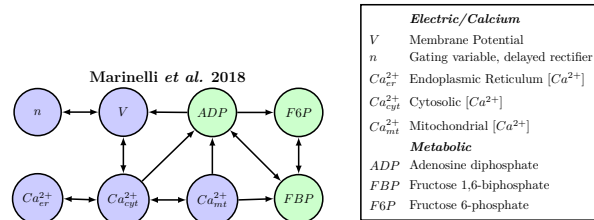


Fig. 1: Network diagram of the 8D Integrated Oscillator Model (IOM) [24], showing the interaction between electrical (blue) and metabolic (green) subsystems.

IOM distinguishes between two metabolic mechanisms: the *Active Metabolic Oscillator* (AMO), driven by intrinsic glycolytic oscillations, and the *Passive Metabolic Oscillator* (PMO), driven by calcium feedback on ATP consumption.

These distinct mechanisms are summarised in Figure 2. The electrical bursts are regulated by Ca^{2+} dynamics, which interlinks the fast electrical and slow metabolic subsystems. As shown in Figure 2, when Ca^{2+} is clamped (light grey background), the metabolic oscillations persist in the AMO regime, revealing its independence. A subsequent clamping of ADP (dark grey background), which clamps ATP as well, confirms that the F6P-FBP AMO is an autonomous oscillator capable of functioning without calcium or ATP feedback. Thus, it can be mathematically isolated from the IOM by clamping both cytosolic Ca^{2+} and ADP, decoupling the electrical and metabolic subsystems. Analysing this isolated AMO is the primary goal of this paper.

The AMO exhibits relaxation oscillations characterised by distinct periods of activity and silence (see Figure 3). This structure indicates inherent multiple timescales. To deconstruct these dynamics, we employ Geometric Singular Perturbation Theory (GSPT), see [8, 15, 16, 20, 4, 27, 22, 28], an approach previously applied to other glycolytic models, such as the Goldbeter-Lefever model for yeast glycolysis [16, 9]. See [2] for an alternative approach to fast-slow analysis in multiple-timescale systems.

However, the analysis of the yeast model does not directly transfer to the β -cell. The Goldbeter-Lefever model relies on allosteric regulation where the enzyme phosphofructokinase (PFK) is activated by its product (ADP) and inhibited by its substrate (ATP). In contrast, the β -cell AMO is derived from the Smolen model [26] for skeletal muscle PFK. Here, while ATP still acts as an inhibitor, the primary driver of oscillation is through a substrate depletion mechanism due to a positive feedback loop from the product Fructose-1,6-bisphosphate (FBP). Although non-dimensionalisation reveals formal similarities between the systems, this distinct biochemical feedback mechanism places the AMO in a different parameter regime with a unique singular geometry that requires specific analysis.

The outline of the paper is as follows: In section 2, we introduce the biophysical AMO model and perform the non-dimensionalisation, identifying the key small parameter ε . We then apply a coordinate change and time-rescaling to transform the system into a polynomial vector field suitable for GSPT analysis. In section 3, we conduct a GSPT analysis by defining three distinct scaling regimes to heuristically construct the singular limit cycle. In section 4, we provide the formal proof for this structure by performing two successive cylindrical blow-ups to rigorously desingularise the degenerate manifolds and prove the transitions between regimes. We conclude in section 5 with a discussion of our findings.

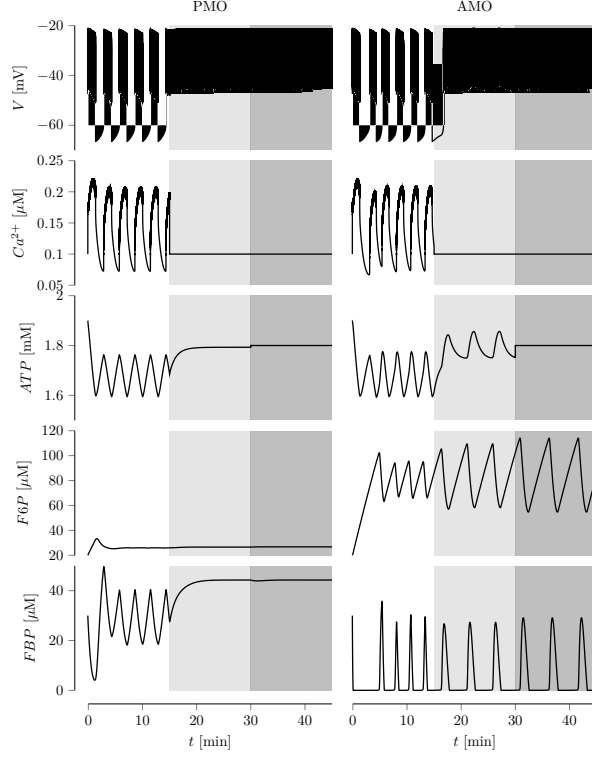


Fig. 2: The dynamics of PMO ($vpdh = 0.0018$) and AMO ($vpdh = 0.009$) in the IOM [24]. Dynamics are shown under Ca^{2+} clamping (light grey) and subsequent ADP clamping (dark grey).

2 The AMO model We embark on our analysis by isolating the AMO from the broader IOM framework. This is achieved by clamping (fixing) cytosolic Ca^{2+} and the ATP/ADP ratio. While in the full IOM the AMO is characterised by autonomous oscillations involving F6P, FBP, and the adenylate charge, we further fix the ATP/ADP ratio to identify the minimal mechanism required for metabolic pulsatility. By doing so, we demonstrate that the internal feedback between the glycolytic intermediates alone is sufficient to sustain the rhythm, identifying the PFK-mediated FBP positive feedback loop as the primary generator of the AMO. This procedure reduces the metabolic oscillator to a two-dimensional system, which we term the ‘self-driven’ AMO. The corresponding biophysical model is described by the following system [24, 1]:

$$(2.1) \quad \left. \begin{aligned} \frac{dx}{dt} &= \beta(\alpha - \nu r(x, y; K)) \\ \frac{dy}{dt} &= \eta(\nu r(x, y; K) - \gamma \sqrt{\frac{y}{\omega}}) \end{aligned} \right\}$$

$$(2.2) \quad r(x, y; K) = \frac{\frac{x^2 y}{\kappa_5} + \frac{x^2}{\kappa_6}}{\frac{x^2 y}{\kappa_1} + \frac{x^2}{\kappa_2} + \frac{y}{\kappa_3} + \frac{1}{\kappa_4}}$$

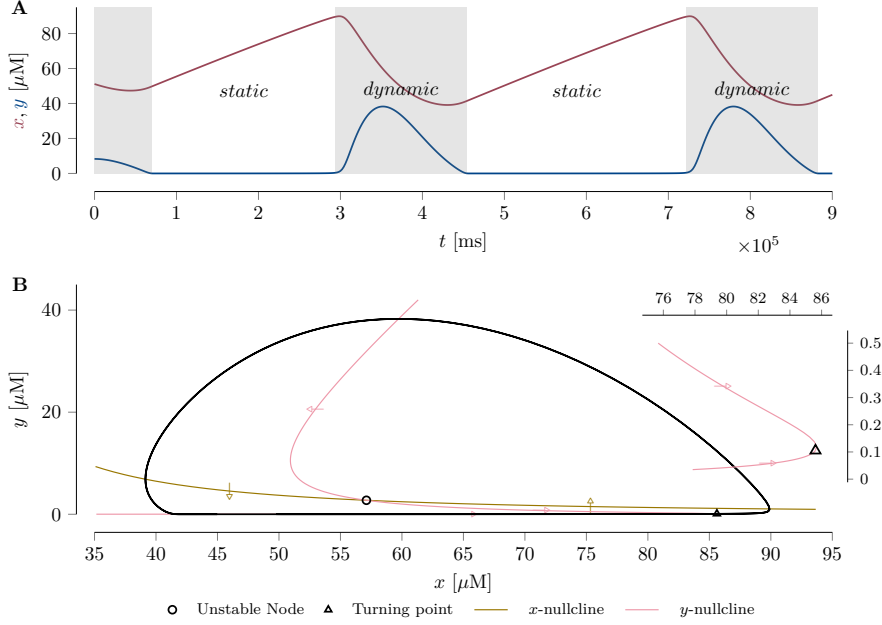


Fig. 3: Original Problem, biophysical System x – y (2.1). **A**: time traces, with dynamic and static phases, Oscillation with a period of $T_{xy} = 4.28 \times 10^5$ ms = 7.125 min. **B**: solid black - phase plot of trajectory.

with state variables $x = \text{F6P}$ and $y = \text{FBP}$, given in units of μM , system parameters $(\alpha, \beta, \eta, \nu, \omega)$ and $K = (\kappa_1, \dots, \kappa_6)$, and flux functions J_{GK}, J_{PFK} and J_{PDH} defined in subsection A.3. Table 5 in subsection A.3 provides the corresponding parameter values with ATP fixed at $1800 \mu\text{M}$.

In Figure 3, the time-traces of the AMO model (2.1) show the structure of a ‘two-stroke’ oscillator [14] comprising a static phase and a dynamic phase, i.e., for low values of y , the dynamics around the y –nullcline informs the static regime while the dynamic regime is a resetting mechanism due to an unstable node (o). The transition from static to dynamic regimes is related to the lower turning (or fold) point (Δ) of the y –nullcline (see inset and contrast scales) which is located close to $y \approx 0$ while the maximum y -value of the observed two-stroke oscillations are a couple of orders of magnitude larger. All of these observations are strong indicators of an inherent multiple timescale structure in the biological processes of the AMO.

2.1 The dimensionless model: To identify processes evolving on different timescales in this AMO, we non-dimensionalise the model (2.1) and identify key small parameters; see, e.g. [13]. This is done by rescaling the dependent and independent variables (x, y, t) :

$$(2.3) \quad x = \kappa_X X, \quad y = \kappa_Y Y, \quad t = \kappa_\tau \tau,$$

where X, Y and τ are the new dimensionless quantities with κ_X, κ_Y and κ_τ as reference scales with the same units as their biophysical counterparts. This gives the corresponding dimensionless AMO:

$$(2.4) \quad \left. \begin{aligned} \frac{dX}{d\tau} &= \hat{\alpha} - \hat{\nu}_1 \hat{r}(X, Y; \Sigma) \\ \frac{dY}{d\tau} &= \hat{\nu}_2 \hat{r}(X, Y; \Sigma) - \hat{\gamma} \sqrt{Y} \end{aligned} \right\}$$

$$(2.5) \quad \hat{r}(X, Y; \Sigma) := \frac{X^2 Y + \hat{\sigma}_6 X^2}{\hat{\sigma}_1 X^2 Y + \hat{\sigma}_2 X^2 + \hat{\sigma}_3 Y + \hat{\sigma}_4}$$

with dimensionless bivariate polynomial $\hat{r}(X, Y; \Sigma)$, dimensionless parameters $\Sigma = (\hat{\sigma}_1, \dots, \hat{\sigma}_4, \hat{\sigma}_6)$ and $(\hat{\alpha}, \hat{\nu}_1, \hat{\nu}_2, \hat{\gamma})$; see Table 1 for the algebraic expressions of all these dimensionless parameters.

Table 1: Dimensionless Parameters for System (2.4).

Par.	Expr.	Par.	Expr.	Par.	Expr.	Par.	Expr.	Par.	Expr.
$\hat{\sigma}_1$	$\frac{\kappa_5}{\kappa_1}$	$\hat{\sigma}_2$	$\frac{\kappa_5}{\kappa_2 \kappa_Y}$	$\hat{\sigma}_3$	$\frac{\kappa_5}{\kappa_3 \kappa_X^2}$	$\hat{\sigma}_4$	$\frac{\kappa_5}{\kappa_4 \kappa_X^2 \kappa_Y}$	$\hat{\sigma}_6$	$\frac{\kappa_5}{\kappa_6 \kappa_Y}$
$\hat{\alpha}$	$\frac{\beta \alpha}{\kappa_\tau \kappa_X}$	$\hat{\nu}_1$	$\frac{\beta \nu}{\kappa_\tau \kappa_X}$	$\hat{\nu}_2$	$\frac{\eta \nu}{\kappa_\tau \kappa_Y}$	$\hat{\gamma}$	$\frac{\eta \gamma}{\kappa_\tau \sqrt{\kappa_Y \omega}}$		

The choice of reference scales is not unique; a meaningful selection should recast system (2.4) into a multiple timescale problem that preserves the AMO's key features. To identify a key small parameter for a perturbation analysis, we specifically selected the following scales:

$$(2.6) \quad \kappa_X = \left(\frac{\kappa_5}{\kappa_4} \right)^{\frac{1}{3}} \left(\frac{\kappa_6^3}{\kappa_4 \kappa_5^2} \right)^{\frac{1}{12}}, \quad \kappa_Y = \left(\frac{\kappa_5}{\kappa_4} \right)^{\frac{1}{3}}, \quad \kappa_\tau = \frac{1}{\eta \nu} \left(\frac{\kappa_5}{\kappa_4} \right)^{\frac{1}{3}}.$$

This choice leads to the dimensionless parameter values summarised in Table 2, and it identifies $\hat{\sigma}_6 = 2.52 \times 10^{-3} \ll 1$ as this key small parameter. Note from Table 2 that the dimensionless parameters $\hat{\alpha}, \hat{\nu}_1, \hat{\sigma}_2, \hat{\sigma}_3$ and $\hat{\sigma}_4$ are all correlated to $\hat{\sigma}_6$. In particular, in the asymptotic limit $\hat{\sigma}_6 \rightarrow 0$, we assume that all these parameters also tend to zero, although at different speeds. We use numerical order of magnitude comparisons to relate the above small parameters which are expressed as algebraic functions with respect to a single small parameter [13], here taken as $\hat{\sigma}_6$. Note that parameters $\hat{\gamma}$ and $\hat{\sigma}_1$ are considered to be of order $\mathcal{O}(1)$.¹

The AMO persists for any $\hat{\sigma}_6 > 0$, but the system's geometry degenerates when $\hat{\sigma}_6 \rightarrow 0$; this defines system (2.4) as a singular perturbation problem. To verify that this is a meaningful limit, we must show that it preserves the key geometric features of the oscillator: (i) a compact domain and confined fold points, and (ii) a unique unstable node.

2.1.1 Compact domain and confined fold points: We start with the Y -nullcline defined by

$$(2.7) \quad X^2 = \frac{\hat{\gamma} Y^{\frac{1}{2}} (\hat{\sigma}_3 Y + \hat{\sigma}_4)}{-\hat{\gamma} \hat{\sigma}_1 Y^{\frac{3}{2}} + Y - \hat{\gamma} \hat{\sigma}_2 Y^{\frac{1}{2}} + \hat{\sigma}_6}.$$

¹Our approach differs from the one performed in [25], where their non-dimensionalisations mainly involved dividing by typical values or upper bounds or time scales.

Table 2: Scaling factors and parameters for non-dimensionalised System (2.4).

Par	Exp	Value	Par	Exp	Value
$\hat{\alpha}$	$\frac{\beta\alpha}{\eta\nu} \left(\frac{\kappa_4\kappa_5^2}{\kappa_6^3} \right)^{\frac{1}{12}}$	5.56×10^{-3}	$\hat{\sigma}_1$	$\frac{\kappa_5}{\kappa_1}$	1.38×10^0
$\hat{\nu}_1$	$\frac{\beta}{\eta} \left(\frac{\kappa_4\kappa_5^2}{\kappa_6^3} \right)^{\frac{1}{12}}$	6.72×10^{-2}	$\hat{\sigma}_2$	$\left(\frac{\kappa_6}{\kappa_2} \right) \left(\frac{\kappa_4\kappa_5^2}{\kappa_6^3} \right)^{\frac{1}{3}}$	4.20×10^{-2}
$\hat{\nu}_2$	1	1.00×10^0	$\hat{\sigma}_3$	$\left(\frac{\kappa_4^2\kappa_5}{\kappa_3^3} \right)^{\frac{1}{3}} \left(\frac{\kappa_4\kappa_5^2}{\kappa_6^3} \right)^{\frac{1}{6}}$	1.14×10^{-1}
$\hat{\gamma}$	$\frac{\gamma}{\nu\sqrt{\omega}} \left(\frac{\kappa_5}{\kappa_4} \right)^{\frac{1}{6}}$	3.30×10^{-1}	$\hat{\sigma}_4$	$\left(\frac{\kappa_4\kappa_5^2}{\kappa_6^3} \right)^{\frac{1}{6}}$	5.02×10^{-2}
			$\hat{\sigma}_6$	$\left(\frac{\kappa_4\kappa_5^2}{\kappa_6^3} \right)^{\frac{1}{3}}$	2.52×10^{-3}

Asymptotic Y-bounds: We require $X^2 \geq 0$. While the numerator of the Y -nullcline is non-negative, the denominator can change sign. The relevant biophysical region of the nullcline is where the denominator is non-negative, bounded by its zeros. We first find these zeros (poles of (2.7)):

$$(2.8) \quad Y^{\frac{3}{2}} - \frac{1}{\hat{\gamma}\hat{\sigma}_1}Y + \frac{\hat{\sigma}_2}{\hat{\sigma}_1}Y^{\frac{1}{2}} - \frac{\hat{\sigma}_6}{\hat{\gamma}\hat{\sigma}_1} = 0.$$

In the asymptotic limit $\hat{\sigma}_6 \rightarrow 0$,² the roots are $Y = 0$ and $Y = (1/\hat{\gamma}\hat{\sigma}_1)^2$. For the corresponding perturbed roots, we use asymptotic approximations (dominant balance): a root close to $Y = 0$ is approximately given by

$$(2.9) \quad Y \approx \left(\frac{\hat{\sigma}_6}{\hat{\gamma}\hat{\sigma}_2} \right)^2.$$

To ensure this root is asymptotically small (as assumed by the asymptotic approximation), the ratio $\hat{\sigma}_6/\hat{\sigma}_2$ must be asymptotically small. This gives a first scaling relationship:

$$(2.10) \quad \hat{\sigma}_2 \sim \mathcal{O}(\hat{\sigma}_6^a), \quad \text{for } 0 < a < 1.$$

A root close to $Y = (1/\hat{\gamma}\hat{\sigma}_1)^2 \sim \mathcal{O}(1)$ is given approximately by

$$(2.11) \quad Y \approx \left(\frac{1}{\hat{\gamma}\hat{\sigma}_1} \right)^2 - 2\frac{\hat{\sigma}_2}{\hat{\sigma}_1} + 2\hat{\gamma}\hat{\sigma}_6 \approx \left(\frac{1}{\hat{\gamma}\hat{\sigma}_1} \right)^2 - 2\frac{\hat{\sigma}_2}{\hat{\sigma}_1},$$

due to (2.10). Thus $Y_{max} = (1/\hat{\gamma}\hat{\sigma}_1)^2$ provides an upper limit on the maximum Y -value of the limit cycle which is achieved when the trajectory crosses the Y -nullcline (horizontal nullcline).

Location of fold points: The S-shaped Y -nullcline has two fold points; their Y -coordinates are defined by the quartic,

$$(2.12) \quad Y^2 + 2\hat{\gamma} \left(\frac{\hat{\sigma}_1\hat{\sigma}_4}{\hat{\sigma}_3} - \hat{\sigma}_2 \right) Y^{\frac{3}{2}} + \left(3\hat{\sigma}_6 - \frac{\hat{\sigma}_4}{\hat{\sigma}_3} \right) Y + \frac{\hat{\sigma}_4\hat{\sigma}_6}{\hat{\sigma}_3} = 0.$$

²By assumption, this implies $\hat{\sigma}_i \rightarrow 0$ for $i = 2, 3, 4$ too.

We require the upper fold's Y -coordinate (Y_{f2}) and the lower fold's X -coordinate (X_{f1}) to be bounded away from zero, i.e., $Y_{f2} \sim \mathcal{O}(1)$ and $X_{f1} \sim \mathcal{O}(1)$.

1. *Upper Fold* (Y_{f2}):

In the asymptotic limit $\hat{\sigma}_6 \rightarrow 0$, the quartic equation (2.12) has a non-trivial approximation

$$(2.13) \quad Y_{f2} + 2\hat{\gamma} \frac{\hat{\sigma}_1 \hat{\sigma}_4}{\hat{\sigma}_3} Y_{f2}^{\frac{1}{2}} - \frac{\hat{\sigma}_4}{\hat{\sigma}_3} \approx 0$$

under the asymptotic assumption³ that the small parameters $\hat{\sigma}_3$ and $\hat{\sigma}_4$ have the same asymptotic scaling, i.e.,

$$(2.14) \quad \frac{\hat{\sigma}_4}{\hat{\sigma}_3} \sim \mathcal{O}(1).$$

Since the two lumped coefficients of (2.13) are assumed $\mathcal{O}(1)$, the unique positive root Y_{f2} is then also $\mathcal{O}(1)$ and given by

$$(2.15) \quad Y_{f2}^{\frac{1}{2}} = \sqrt{\left(\frac{\hat{\gamma} \hat{\sigma}_1 \hat{\sigma}_4}{\hat{\sigma}_3}\right)^2 + \frac{\hat{\sigma}_4}{\hat{\sigma}_3}} - \frac{\hat{\gamma} \hat{\sigma}_1 \hat{\sigma}_4}{\hat{\sigma}_3}.$$

Substituting (2.15) into the Y -nullcline equation (2.7) shows that the corresponding X -coordinate, X_{f2} vanishes in the asymptotic limit $\hat{\sigma}_6 \rightarrow 0$, i.e., $X_{f2} \sim \mathcal{O}(\hat{\sigma}_3^{\frac{1}{2}}, \hat{\sigma}_4^{\frac{1}{2}}) \rightarrow 0$.

2. *Lower Fold* (X_{f1}):

For the asymptotically small root of the quartic (2.12), Y_{f1} , the lowest order terms provide the dominant balance, giving the leading-order approximation for the lower fold's Y -coordinate:

$$(2.16) \quad Y_{f1} \approx \hat{\sigma}_6.$$

Substituting (2.16) into the Y -nullcline equation (2.7) leads to the leading-order approximation

$$(2.17) \quad X_{f1}^2 \approx \frac{\hat{\gamma} \hat{\sigma}_4 \sqrt{\hat{\sigma}_6}}{2\hat{\sigma}_6 - \hat{\gamma} \hat{\sigma}_2 \sqrt{\hat{\sigma}_6}}.$$

For X_{f1} to be non-negative, this requires $2\hat{\sigma}_6 > \hat{\gamma} \hat{\sigma}_2 \sqrt{\hat{\sigma}_6}$, which imposes a new lower bound on the exponent in the scaling (see (2.10)), $\hat{\sigma}_2 \sim \mathcal{O}(\hat{\sigma}_6^a) : \frac{1}{2} < a < 1$. This condition can be relaxed to $1/2 \leq a < 1$, i.e.,

$$(2.18) \quad \hat{\sigma}_2 \sim \mathcal{O}(\hat{\sigma}_6^a) : \frac{1}{2} \leq a < 1,$$

with the border case $a = 1/2$ requiring the additional constraint

$$(2.19) \quad \sigma_2 := \frac{\hat{\sigma}_2}{\sqrt{\hat{\sigma}_6}} < \frac{2}{\hat{\gamma}}$$

which is satisfied based on Table 2.

For X_{f1} to be bounded away from zero, i.e., $X_{f1}^2 \sim \mathcal{O}(1)$, the numerator and denominator of (2.17) must vanish at the same rate. Since $1/2 \leq a < 1$, the denominator is of order $\mathcal{O}(\hat{\sigma}_6)$. The numerator is of order $\mathcal{O}(\hat{\sigma}_4 \sqrt{\hat{\sigma}_6})$. The balance $\mathcal{O}(\hat{\sigma}_4 \sqrt{\hat{\sigma}_6}) = \mathcal{O}(\hat{\sigma}_6)$, in conjunction with (2.14), requires the asymptotic scaling:

$$(2.20) \quad \hat{\sigma}_4 \sim \mathcal{O}(\hat{\sigma}_6^{\frac{1}{2}}) \Rightarrow \hat{\sigma}_3 \sim \mathcal{O}(\hat{\sigma}_6^{\frac{1}{2}}).$$

³Recall that $\hat{\gamma}$ and $\hat{\sigma}_1$ are $\mathcal{O}(1)$.

2.1.2 The unstable node: The X -nullcline is defined by

$$(2.21) \quad X^2 = \frac{\hat{\alpha}(\hat{\sigma}_3 Y + \hat{\sigma}_4)}{(\hat{\nu}_1 - \hat{\alpha}\hat{\sigma}_1)Y + (\hat{\nu}_1\hat{\sigma}_6 - \hat{\alpha}\hat{\sigma}_2)}.$$

Equating (2.7) and (2.21) gives the following unique equilibrium

$$(2.22) \quad (X_{eq}, Y_{eq}) = \left(\left(\frac{\hat{\alpha}(\hat{\alpha}^2\hat{\sigma}_3 + \hat{\gamma}^2\hat{\nu}_1^2\hat{\sigma}_4)}{\hat{\gamma}^2\hat{\nu}_1^2(\hat{\nu}_1\hat{\sigma}_6 - \hat{\alpha}\hat{\sigma}_2) + \hat{\alpha}^2(\hat{\nu}_1 - \hat{\alpha}\hat{\sigma}_1)} \right)^{1/2}, \left(\frac{\hat{\alpha}}{\hat{\gamma}\hat{\nu}_1} \right)^2 \right).$$

We require this equilibrium to lie on the middle branch of the Y -nullcline between the two fold points, i.e. $Y_{f1} < Y_{eq} < Y_{f2}$, which guarantees that it is an unstable node (see subsection A.4 for details). A necessary condition for $Y_{eq} > Y_{f1}$ to be bounded away from zero in the asymptotic limit $\hat{\sigma}_6 \rightarrow 0$,⁴ is given by

$$(2.23) \quad \frac{\hat{\nu}_1}{\hat{\alpha}} \sim \mathcal{O}(1).$$

Thus, we assume $\hat{\alpha}, \hat{\nu}_1 \sim \mathcal{O}(\hat{\sigma}_6^b)$ for $b \in (0, 1)$. Under this condition, $Y_{f1} < Y_{eq}$ is asymptotically satisfied as $Y_{f1} \rightarrow 0$ while $Y_{eq} \sim \mathcal{O}(1)$. To guarantee a non-negative X_{eq} value, we need the additional condition $\hat{\nu}_1 > \hat{\alpha}\hat{\sigma}_1$. The final asymptotic condition to check is $Y_{eq} < Y_{f2}$. This inequality, after substituting Y_{eq} and Y_{f2} from (2.22) and (2.15) respectively, simplifies to the necessary condition:

$$(2.24) \quad \left(\frac{\hat{\alpha}}{\hat{\gamma}\hat{\nu}_1} \right)^2 \left(1 - 2\hat{\sigma}_1 \frac{\hat{\alpha}}{\hat{\nu}_1} \right)^{-1} < \frac{\hat{\sigma}_4}{\hat{\sigma}_3}$$

which requires the updated final condition on the parameters $\hat{\nu}_1$, $\hat{\alpha}$ and $\hat{\sigma}_1$:

$$(2.25) \quad \frac{\hat{\nu}_1}{\hat{\alpha}} > 2\hat{\sigma}_1.$$

These two conditions (2.24) and (2.25) are satisfied by looking at Table 2.

2.1.3 Comparison with system parameters: We compare the derived asymptotic hierarchy with the formulas for the dimensionless system parameters in Table 2. This allows us to determine the ‘best choice’ for the free exponents and confirm the consistency of the entire analysis.

Table 2 shows that all small parameters are correlated through $\hat{\sigma}_6$, and we define $\varepsilon := \hat{\sigma}_6^{\frac{1}{4}}$. Both $\hat{\sigma}_3$ and $\hat{\sigma}_4$ are proportional to ε^2 , which perfectly matches (2.20). In fact, $\hat{\sigma}_4 = \varepsilon^2$ based on Table 2. Likewise, $\hat{\alpha}$ and $\hat{\nu}_1$ are proportional to ε , which would correspond to $b = \frac{1}{4}$, see (2.23), giving $\hat{\alpha}, \hat{\nu}_1 \sim \mathcal{O}(\varepsilon)$. The prefactors of the above four small parameters are considered to be of order $\mathcal{O}(1)$.

We still have freedom in the exponent a of the $\hat{\sigma}_2$ scaling (2.18), and we choose $a = 1/2$. For this scaling $\hat{\sigma}_2 \sim \mathcal{O}(\sqrt{\hat{\sigma}_6})$ (i.e., $a = 1/2$) to hold, the expression for $\hat{\sigma}_2$ in Table 2 implies a constraint on the underlying biophysical parameters (κ_2, κ_6) . Specifically, since $\hat{\sigma}_2 = (\kappa_6/\kappa_2)\hat{\sigma}_6$, the ratio κ_6/κ_2 must scale as $\mathcal{O}(\hat{\sigma}_6^{-1/2})$ or, equivalently, $\mathcal{O}(\varepsilon^{-2})$.

⁴Recall, this also implies $\hat{\alpha} \rightarrow 0$ and $\hat{\nu}_1 \rightarrow 0$.

Remark 2.1. The asymptotic condition (2.18) implies a tight relationship between the biophysical parameters κ_2 and κ_6 , which indeed differ by a single term in the weights from the Smolen model, from which system (2.1) is derived. Thus, the asymptotic condition (2.18) can also be justified from a modeling point of view.

Altogether, this gives the resulting hierarchy of identified small parameters

$$(2.26) \quad \begin{aligned} \hat{\sigma}_6 &= \varepsilon^4 \\ \hat{\sigma}_2, \hat{\sigma}_3, \hat{\sigma}_4 &\sim \mathcal{O}(\varepsilon^2) \\ \hat{\alpha}, \hat{\nu}_1 &\sim \mathcal{O}(\varepsilon) \end{aligned}$$

Remark 2.2. The asymptotic relationships among $\hat{\sigma}_3$, $\hat{\sigma}_4$ and $\hat{\sigma}_6$ suggest potential connections among the biophysical parameters, which are derived from the Smolen weights (see (A.9) in subsection A.3). Note that the different $\hat{\sigma}$'s may pairwise share different biophysical parameters, not necessarily all, based on the indices $i, j, k, l \in \{0, 1\}$. In the asymptotic limit the non-dimensionalised small parameter $\hat{\sigma}_6 \rightarrow 0$, some constituent biophysical parameters in the Smolen weight are either asymptotically approaching 0 or ∞ . The set of the latter asymptotic biophysical parameters is constrained by the independence of $\hat{\sigma}_1 \sim \mathcal{O}(1)$ wrt the asymptotic limit $\hat{\sigma}_6 \rightarrow 0$. We tested this biophysical constraint against all the parameters in the Smolen weights and found that in the asymptotic limit $f_{23} \rightarrow \infty$, the above conditions are satisfied.

With all these asymptotic relationships, coupled with a little abuse of notation by dropping the \hat and \sim from all parameters as well as the subscript in $\hat{\nu}_1$, we transform system (2.4) to the singularly perturbed AMO

$$(2.27) \quad \left. \begin{aligned} \frac{dX}{d\tau} &= \varepsilon \left(\alpha - \nu \frac{X^2 Y + \varepsilon^4 X^2}{\sigma_1 X^2 Y + \varepsilon^2 (\sigma_2 X^2 + \sigma_3 Y + 1)} \right) \\ \frac{dY}{d\tau} &= \frac{X^2 Y + \varepsilon^4 X^2}{\sigma_1 X^2 Y + \varepsilon^2 (\sigma_2 X^2 + \sigma_3 Y + 1)} - \gamma \sqrt{Y} \end{aligned} \right\}$$

The singular nature of the AMO is revealed in Figure 4 where we simulated system (2.27) with decreasing values of ε . In the limit $\varepsilon \rightarrow 0$, the limit cycle approaches the rectangular box (dashed black box) and the frequency approaches zero which indicates an ε -dependent frequency. The rectangular box also represents the compact domain that emerged from the asymptotic boundedness conditions we imposed. In the middle panel of Figure 4, we further observe that the unstable node (\circ) converges to the point $(0, Y_{eq})$ on the Y -axis, where $Y_{eq} \sim \mathcal{O}(1)$. In contrast, looking at the bottom panel of Figure 4, the lower fold point (X_{f1}, Y_{f1}) converges to a point on the X -axis, as its coordinates approach $(X_{f1,0}, 0)$ where $X_{f1,0} \sim \mathcal{O}(1)$. Both of these observations highlight the singular nature of the AMO.

2.1.4 Dealing with the square root: In system (2.27), we notice that $Y = 0$ constitutes a singularity due to the \sqrt{Y} term with its infinite slope at $Y = 0$. We use a two-step transformation process to deal with this singularity. In a first step, we perform the coordinate transformation $Y = Z^2$ to obtain a (now) rational vector field

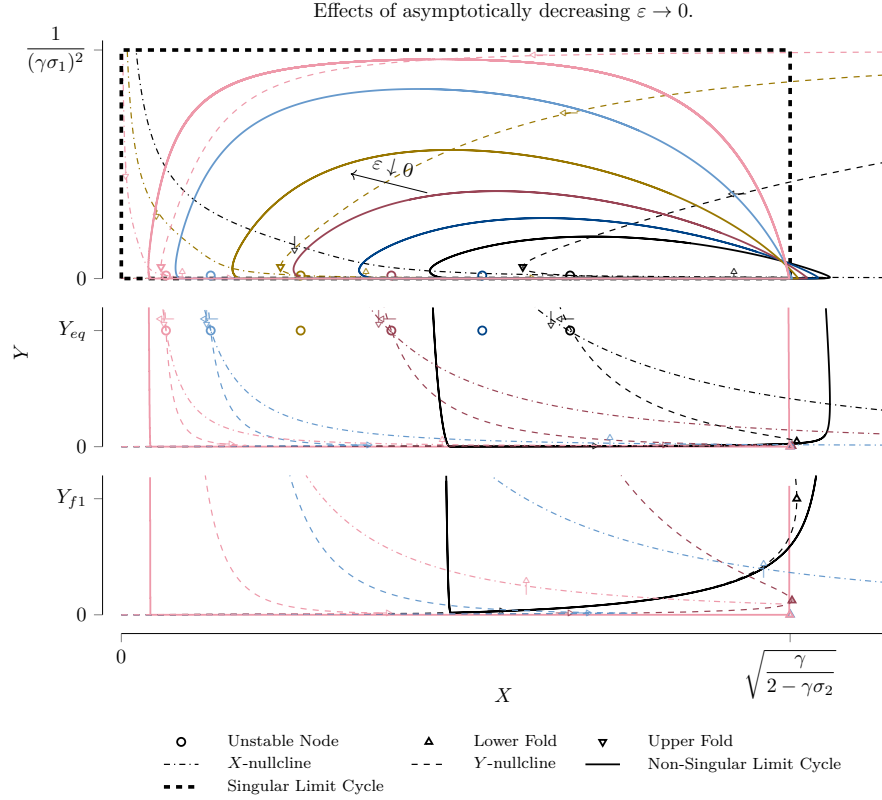


Fig. 4: Nondimensionalised System X-Y (2.27): *Top*: Phase plane showing limit cycles. *Middle*: Zoomed view showing convergence of the equilibrium point \circ at $\mathcal{O}(Y_{eq})$ scale. *Bottom*: Zoomed view showing convergence of the fold point Δ at $\mathcal{O}(Y_{f1})$ scale.

$$(2.28) \quad \left. \begin{aligned} \frac{dX}{d\tau} &= \varepsilon \left(\alpha - \nu \frac{X^2 Z^2 + \varepsilon^4 X^2}{\sigma_1 X^2 Z^2 + \varepsilon^2 (\sigma_2 X^2 + \sigma_3 Z^2 + 1)} \right) \\ \frac{dZ}{d\tau} &= \frac{1}{2Z} \left(\frac{X^2 Z^2 + \varepsilon^4 X^2}{\sigma_1 X^2 Z^2 + \varepsilon^2 (\sigma_2 X^2 + \sigma_3 Z^2 + 1)} - \gamma Z \right) \end{aligned} \right\}$$

which exposes the said singularity at $Z = 0$ in its denominator.

In a second step, we make a state-dependent (nonlinear) time transformation⁵

$$(2.29) \quad d\tau = 2Z (\sigma_1 X^2 Z^2 + \varepsilon^2 (\sigma_2 X^2 + \sigma_3 Z^2 + 1)) d\bar{\tau}$$

to obtain a polynomial vector field from system (2.28):

$$(2.30) \quad \left. \begin{aligned} X' &= -2\varepsilon Z ((\nu - \alpha\sigma_1)X^2 Z^2 - \varepsilon^2 \alpha (\sigma_2 X^2 + \sigma_3 Z^2 + 1) + \varepsilon^4 \nu X^2) \\ Z' &= (1 - \gamma\sigma_1 Z)X^2 Z^2 - \varepsilon^2 \gamma Z (\sigma_2 X^2 + \sigma_3 Z^2 + 1) + \varepsilon^4 X^2 \end{aligned} \right\}$$

⁵This transformation is, by its nature, singular at $Z = 0$.

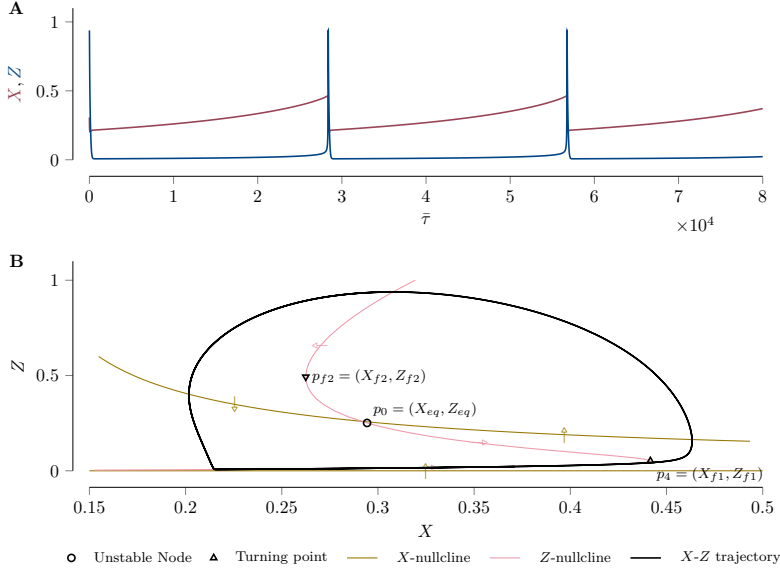


Fig. 5: Relaxation Oscillator: System X-Z (2.30): *upper*: time trace, *lower*: phase plot.

where $'$ denotes differentiation wrt $\bar{\tau}$. Note that the singularity at $Z = 0$ of the $dZ/d\bar{\tau}$ -equation in (2.28) has now become an additional nullcline of the X' -equation in (2.30).

As expected, this new system (2.30) no longer has the two-stroke structure comprising a static phase and a dynamic phase as in Figure 3, but rather exhibits typical relaxation oscillator dynamics, evolving on multiple timescales, see Figure 5. The concomitant stretching of the slow phase and the shrinkage of the fast phase are a direct consequence of the state-dependent time transformation (2.29).

We have thus finished the pre-processing of the AMO model, arriving at a non-dimensionalised system (2.30) with a singular perturbation parameter $\varepsilon \ll 1$ that is amenable to GSPT analysis. The asymptotic analysis from subsections 2.1.1 and 2.1.2 already reveals the singular geometry of this system in the limit $\varepsilon \rightarrow 0$. The key geometric features collapse onto the coordinate axes:

- *The unstable node p_0* : $(X_{eq}, Z_{eq}) \sim (\mathcal{O}(\varepsilon), \mathcal{O}(1))$. It converges to $(0, Z_{eq,0})$ on the Z -axis, where $Z_{eq,0} = \alpha/(\gamma\nu)$ (from (2.22)).
- *The lower fold p_4* : $(X_{f1}, Z_{f1}) \sim (\mathcal{O}(1), \mathcal{O}(\varepsilon^2))$. It converges to $(X_{f1,0}, 0)$ on the X -axis. Its $\mathcal{O}(1)$ coordinate is $X_{f1,0}^2 = \gamma/(2 - \gamma\sigma_2)$, as derived from (2.17) and the final hierarchy in (2.26) (where $\hat{\sigma}_4 = \varepsilon^2$).
- *The upper fold p_{f2}* : $(X_{f2}, Z_{f2}) \sim (\mathcal{O}(\varepsilon), \mathcal{O}(1))$. It also converges to the Z -axis at $(0, Z_{f2,0})$, where $Z_{f2,0} = \sqrt{Y_{f2,0}} \sim \mathcal{O}(1)$ is the explicit $\mathcal{O}(1)$ root given by (2.15).

This collapse is also seen in the nullclines. In the singular limit, the X' -nullcline ((2.30), $X' = 0$) degenerates to the axes $Z = 0$ and $X = 0$. The Z' -nullcline ($Z' = 0$) degenerates to $Z = 0$, $X = 0$, and the line $Z = 1/(\gamma\sigma_1)$. The extensive overlap on the axes highlights the degeneracy of the singular problem. This multi-scale singular structure, where features exist at $\mathcal{O}(1)$, $\mathcal{O}(\varepsilon)$ and $\mathcal{O}(\varepsilon^2)$ scales, dictates our GSPT

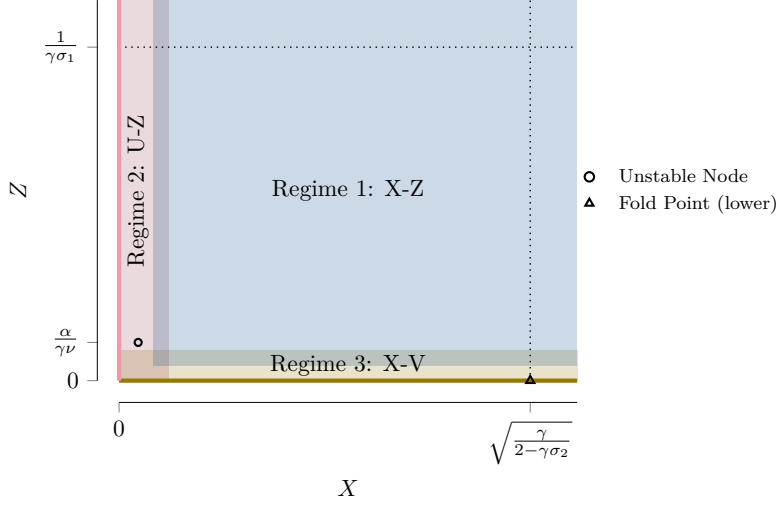


Fig. 6: The three scaling regimes required for the GSPT analysis, as derived from the asymptotic scalings of the equilibrium and fold points.

analysis strategy. We must analyse the system in three distinct scaling regimes, as illustrated in Figure 6:

- *Regime 1* ($X, Z \sim \mathcal{O}(1)$): The ‘outer’ view.
- *Regime 2* ($X = \varepsilon U, Z \sim \mathcal{O}(1)$): A ‘zoom’ near the Z -axis to resolve the unstable node.
- *Regime 3* ($X \sim \mathcal{O}(1), Z = \varepsilon^2 V$): A ‘zoom’ near the X -axis to resolve the lower fold.

3 Scaling regimes analysis: In the following, we analyse the oscillatory dynamics of (2.30) in the three aforementioned scaling regimes by means of the GSPT toolbox (see section B).

3.1 System X-Z (Regime 1): We present system (2.30) in the general form of a singularly perturbed system (see section B for further details):

$$\begin{aligned}
 (3.1) \quad \begin{pmatrix} X' \\ Z' \end{pmatrix} &= \begin{pmatrix} 0 \\ 1 \end{pmatrix} (1 - \gamma\sigma_1 Z) X^2 Z^2 + \varepsilon \begin{pmatrix} -2(\nu - \alpha\sigma_1) X^2 Z^3 \\ 0 \end{pmatrix} \\
 &+ \varepsilon^2 \begin{pmatrix} 0 \\ -\gamma Z(\sigma_2 X^2 + \sigma_3 Z^2 + 1) \end{pmatrix} + \varepsilon^3 \begin{pmatrix} 2\alpha Z(\sigma_2 X^2 + \sigma_3 Z^2 + 1) \\ 0 \end{pmatrix} \\
 &+ \varepsilon^4 \begin{pmatrix} 0 \\ X^2 \end{pmatrix} + \varepsilon^5 \begin{pmatrix} -2\nu X^2 Z \\ 0 \end{pmatrix} := N_0(X, Z) f_0(X, Z) + \sum_{i=1}^5 \varepsilon^i F_i(X, Z),
 \end{aligned}$$

with $N_0(X, Z) = N_0 = (0, 1)^\top$ a constant vector and $f_0(X, Z) = (1 - \gamma\sigma_1 Z) X^2 Z^2$ a scalar function. This form highlights the 6 distinct processes evolving on distinct timescales of $\mathcal{O}(\varepsilon^i)$, $i = 0, 1, \dots, 5$.

3.1.1 The layer problem: The layer problem (see subsection B.1) is obtained by taking the singular limit $\varepsilon \rightarrow 0$ in (3.1), which gives

$$(3.2) \quad \begin{pmatrix} X' \\ Z' \end{pmatrix} = \begin{pmatrix} 0 \\ 1 \end{pmatrix} (1 - \gamma\sigma_1 Z) X^2 Z^2 = N_0 f_0(X, Z).$$

This is a standard singular perturbation problem: X is a constant (and thus identified as a slow variable), Z is the ‘fast’ variable, and the span of N_0 represents the fast fibre of the layer problem. The set of equilibria S_0 of the layer problem is defined by

$$f_0(X, Z) = X^2 Z^2 (1 - \gamma \sigma_1 Z) = 0$$

comprising three one-dimensional branches, i.e.,

$$(3.3) \quad S_0 = \Gamma_0 \cup \Gamma_1 \cup \Gamma_2 = \{Z = 0\} \cup \{X = 0\} \cup \left\{Z = \frac{1}{\gamma \sigma_1}\right\}$$

that pairwise intersect at $\Gamma_0 \cap \Gamma_1 = (0, 0)$ and $p_1 := \Gamma_1 \cap \Gamma_2 = (0, 1/(\gamma \sigma_1))$. Each branch is viewed as a one-dimensional critical manifold of the layer problem. To determine the stability properties of each branch Γ_i , $i = 0, 1, 2$, we calculate the non-trivial eigenvalue:

$$(3.4) \quad \lambda = Df_0 N_0 = D_z f_0 = X^2 Z (2 - 3\gamma \sigma_1 Z).$$

We notice that this eigenvalue vanishes when evaluated along the branches Γ_0 and Γ_1 , and, hence, both branches are degenerate. On the other hand, λ evaluated along Γ_2 gives

$$\lambda\left(X, \frac{1}{\gamma \sigma_1}\right) = -\frac{X^2}{\gamma \sigma_1} \leq 0.$$

Hence, we have $\Gamma_2 = \Gamma_2^{N^-} \cup p_1 \cup \Gamma_2^{N^+}$ with normally hyperbolic branches $\Gamma_2^{N^\pm}$, both attracting, and loss of normal hyperbolicity at p_1 .

3.1.2 The reduced problem along Γ_2 : The corresponding leading order reduced problem (see subsection B.2) along Γ_2 is given by

$$(3.5) \quad \dot{X} = -2(\nu - \alpha \sigma_1) X^2 Z^3|_{\Gamma_2} = -2 \frac{(\nu - \alpha \sigma_1)}{\gamma^3 \sigma_1^3} X^2.$$

Since $\nu > \alpha \sigma_1$, see (2.25), the flow on the slow manifold Γ_2 decreases monotonically towards $X = 0$ for $X > 0$.

3.2 System U-Z (Regime 2): To understand the slow dynamics near the degenerate manifold Γ_1 of the X-Z system (3.1), we zoom in on Regime 2 through the following coordinate and time transformations:

$$(3.6) \quad X := \varepsilon U, \quad d\bar{\tau} = \varepsilon^{-2} d\tau_2.$$

With $' = d/d\tau_2$ and $\tilde{\varepsilon} := \varepsilon^2$, we obtain

$$(3.7) \quad \left. \begin{aligned} U' &= -2Z \left[(\nu - \alpha \sigma_1) U^2 Z^2 - \alpha (\sigma_3 Z^2 + 1) - \tilde{\varepsilon} \alpha \sigma_2 U^2 + \tilde{\varepsilon}^2 \nu U^2 \right] \\ Z' &= (1 - \gamma \sigma_1 Z) U^2 Z^2 - \gamma Z (\sigma_3 Z^2 + 1) - \tilde{\varepsilon} \gamma \sigma_2 U^2 Z + \tilde{\varepsilon}^2 U^2 \end{aligned} \right\}$$

which is a singular perturbation problem but in general, *non-standard form*⁶

$$(3.8) \quad \begin{aligned} \begin{pmatrix} U' \\ Z' \end{pmatrix} &= \begin{pmatrix} -2 \left[(\nu - \alpha \sigma_1) U^2 Z^2 - \alpha (\sigma_3 Z^2 + 1) \right] \\ (1 - \gamma \sigma_1 Z) U^2 Z - \gamma (\sigma_3 Z^2 + 1) \end{pmatrix} Z + \tilde{\varepsilon} \begin{pmatrix} 2\alpha \sigma_2 U^2 Z \\ -\gamma \sigma_2 U^2 Z \end{pmatrix} \\ &+ \tilde{\varepsilon}^2 \begin{pmatrix} -2\nu U^2 Z \\ U^2 \end{pmatrix} := N_0(U, Z) f_0(U, Z) + \sum_{i=1}^2 \tilde{\varepsilon}^i F_i(U, Z), \end{aligned}$$

⁶In non-standard form, there is no explicit identification of slow and fast variables.

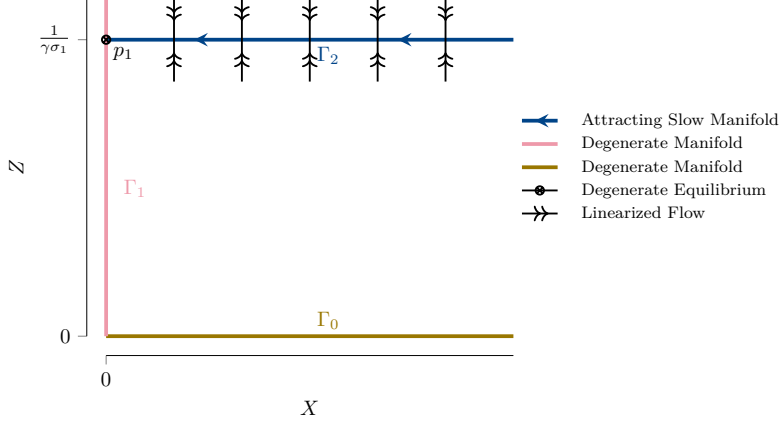


Fig. 7: Analysis of X-Z System (Regime 1), showing the three branches of the critical manifold S_0 and the reduced flow on the attracting branch Γ_2^N .

with state-dependent vector $N_0(U, Z)$ and scalar function $f_0(U, Z) = Z$. This form highlights the 3 distinct processes evolving on the timescales $\mathcal{O}(\varepsilon^i)$, $i = 0, 1, 2$.

3.2.1 The layer problem: The layer problem is obtained by taking the singular limit $\tilde{\varepsilon} \rightarrow 0$ in (3.8), which gives

$$(3.9) \quad \begin{pmatrix} U' \\ Z' \end{pmatrix} = \begin{pmatrix} -2 [(\nu - \alpha\sigma_1)U^2Z^2 - \alpha(\sigma_3Z^2 + 1)] \\ (1 - \gamma\sigma_1Z)U^2Z - \gamma(\sigma_3Z^2 + 1) \end{pmatrix} Z = N_0(U, Z)f_0(U, Z).$$

The set of equilibria S_0 of (3.9) comprises the one-dimensional critical manifold $\Gamma_5 = \{Z = 0\}$ and the single isolated point p_0 at which the vector $N_0(U, Z)$ is singular. For the critical manifold Γ_5 , the Jacobian is given by

$$J(\Gamma_5) = N_0(\Gamma_5)Df_0(\Gamma_5) = \begin{pmatrix} 0 & 2\alpha \\ 0 & -\gamma \end{pmatrix}$$

with the non-trivial eigenvalue $\lambda(\Gamma_5) = -\gamma < 0$, indicating that the critical manifold Γ_5 is uniformly attracting along the eigendirection $[2\alpha, -\gamma]^T$.

To analyse the stability of the equilibrium point p_0 we evaluate the Jacobian:

$$\tilde{J}(U, Z) = DN_0(U, Z)f_0(U, Z) = \begin{pmatrix} -4(\nu - \alpha\sigma_1)UZ^3 & -4((\nu - \alpha\sigma_1)U^2 - \alpha\sigma_3)Z^2 \\ 2(1 - \gamma\sigma_1Z)UZ^2 & ((1 - 2\gamma\sigma_1Z)U^2 - 2\gamma\sigma_3Z)Z \end{pmatrix}$$

with trace $\text{tr}(\tilde{J}(U, Z)) = -4(\nu - \alpha\sigma_1)UZ^3 + [(1 - 2\gamma\sigma_1Z)U^2 - 2\gamma\sigma_3Z]Z$ which expands to:

$$\text{tr}(\tilde{J}(U, Z)) = -4\nu UZ^3 + 4\alpha\sigma_1 UZ^3 + U^2Z - 2\gamma\sigma_1 U^2Z^2 - 2\gamma\sigma_3 Z^2.$$

Since $\det(\tilde{J}(p_0)) > 0$, $\text{tr}(\tilde{J}(p_0)) > 0$ and $\text{tr}(\tilde{J}(p_0))^2 > 4\det(\tilde{J}(p_0))$, we conclude that p_0 is an unstable node (see also subsection A.4).

The layer flow, shown in Figure 8, is determined by the interplay between the unstable node p_0 and the attracting critical manifold Γ_5 . The node p_0 repels all nearby trajectories, which are then drawn towards the uniformly attracting manifold $\Gamma_5 = \{Z = 0\}$. Overall, all trajectories (except the node p_0 itself) eventually approach this attracting manifold, which provides the initial condition for the slow flow.

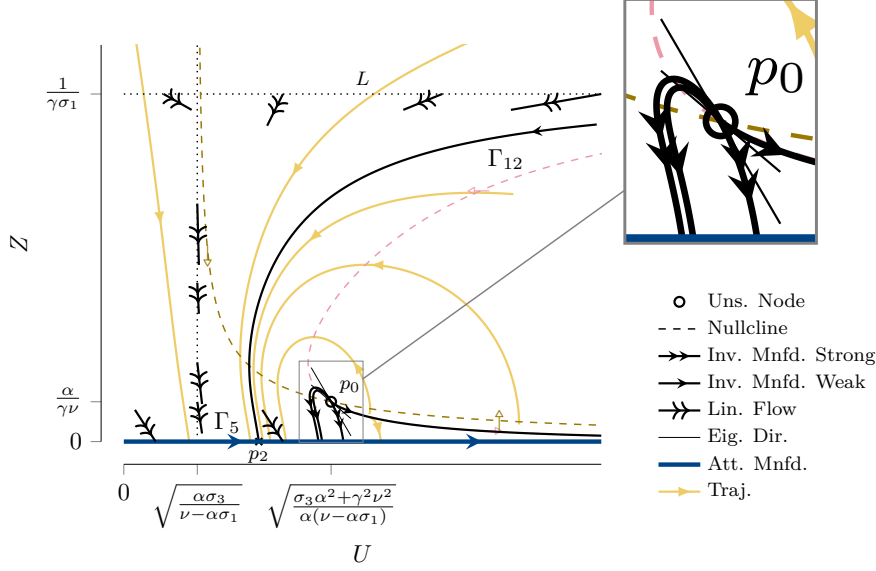


Fig. 8: Analysis of U-Z System (Regime 2). The layer problem (3.9) shows the phase space partitioned by the U -nullcline (olive), Z -nullcline (magenta), and a separatrix Γ_{12} . The flow is dominated by the unstable node p_0 and the attracting manifold $\Gamma_5 = \{Z = 0\}$.

Remark 3.1. While the local layer flow simply approaches Γ_5 , the nullclines and the separatrix Γ_{12} shown in Figure 8 are crucial for understanding the global dynamics. As a later analysis will show, Γ_{12} (Figure 12) is the true extension of the slow flow from the manifold Γ_2 and, hence, also plays an important role in partitioning trajectories arriving from infinity.

3.2.2 The reduced problem: To obtain the slow flow, we introduce the slow timescale $\tilde{\tau}_s$ through $d\tilde{\tau}_s = \tilde{\varepsilon}d\tau_2$, which transforms the fast problem (3.8) into the slow problem

$$\begin{aligned}
 \tilde{\varepsilon} \begin{pmatrix} \dot{U} \\ \dot{Z} \end{pmatrix} &= \underbrace{\begin{pmatrix} -2[(\nu - \alpha\sigma_1)U^2Z^2 - \alpha(\sigma_3Z^2 + 1)] \\ (1 - \gamma\sigma_1Z)U^2Z - \gamma(\sigma_3Z^2 + 1) \end{pmatrix}}_{F_0(U,Z)=N_0(U,Z)f_0(U,Z)} Z + \tilde{\varepsilon} \underbrace{\begin{pmatrix} 2\alpha\sigma_2U^2Z \\ -\gamma\sigma_2U^2Z \end{pmatrix}}_{F_1(U,Z)} \\
 (3.10) \quad &+ \tilde{\varepsilon}^2 \underbrace{\begin{pmatrix} -2\nu U^2Z \\ U^2 \end{pmatrix}}_{F_2(U,Z)} = F(U, Z, \tilde{\varepsilon})
 \end{aligned}$$

where $\dot{\cdot} = d/d\tilde{\tau}_s$. In the singular limit $\tilde{\varepsilon} \rightarrow 0$, this system is only well defined along the critical manifold $\Gamma_5 = \{Z = 0\}$.

The classical Fenichel [8] approach for finding the slow flow along Γ_5 involves projecting the $\mathcal{O}(\tilde{\varepsilon})$ vector field F_1 onto the tangent space of Γ_5 , see Figure 17. However, evaluating F_1 on Γ_5 (where $Z = 0$) gives $F_1(U, 0) = [0, 0]^T$. Thus the slow flow is trivial to order $\mathcal{O}(\tilde{\varepsilon})$.

The parametrisation method: To systematically resolve this and identify the leading order non-trivial flow, we employ the parametrisation method (see section C). This method seeks to find a perturbed slow manifold $\Gamma_{\tilde{\varepsilon}}$ as an embedding $\phi(\xi, \tilde{\varepsilon})$ and a

slow vector field $r(\xi, \tilde{\varepsilon})$ on it, which must satisfy the conjugacy equation:

$$(3.11) \quad \tilde{\varepsilon} D\phi(\xi, \tilde{\varepsilon}) \cdot r(\xi, \tilde{\varepsilon}) = F(\phi(\xi, \tilde{\varepsilon}))$$

where the manifold Γ_5 is parametrised by the (local) coordinate $\xi = U$ as a graph, i.e., $\Gamma_5(\xi) : (U, Z)^\top = (\xi, 0)^\top$. We expand the embedding and the slow vector field as a power series in $\tilde{\varepsilon}$:

$$\begin{aligned} \phi(\xi, \tilde{\varepsilon}) &= \phi_0(\xi) + \tilde{\varepsilon}\phi_1(\xi) + \tilde{\varepsilon}^2\phi_2(\xi) + \mathcal{O}(\tilde{\varepsilon}^3) \\ r(\xi, \tilde{\varepsilon}) &= r_0(\xi) + \tilde{\varepsilon}r_1(\xi) + \tilde{\varepsilon}^2r_2(\xi) + \mathcal{O}(\tilde{\varepsilon}^3) \end{aligned}$$

with $\phi_0(\xi) = [\xi, 0]^\top$. Substituting these into (3.11) and collecting terms by powers of $\tilde{\varepsilon}$ gives a hierarchy of equations.

- *At $\mathcal{O}(\tilde{\varepsilon})$:* We solve $J(\Gamma_5)\phi_1 + F_1(\phi_0) = \phi_0' r_1$. Since $F_1(\phi_0) = 0$, this yields the trivial solution $r_1 = 0$ and $\phi_1 = 0$.
- *At $\mathcal{O}(\tilde{\varepsilon}^2)$:* The equation simplifies to $J(\Gamma_5)\phi_2 + F_2(\phi_0) = \phi_0' r_2$.

Using the graph ansatz $\phi(\xi, \tilde{\varepsilon}) = \phi_0(\xi) + \tilde{\varepsilon}^2(0, f_2(\xi))^\top + \dots$ and the non-trivial contribution $F_2(\phi_0) = [0, \xi^2]^\top$, we solve this second equation (see section C for details). This yields the leading-order non-trivial reduced vector field:

$$(3.12) \quad r_2(\xi) = \frac{2\alpha\xi^2}{\gamma} \geq 0.$$

Thus, the flow on the slow manifold Γ_5 is non-trivial at $\mathcal{O}(\tilde{\varepsilon}^2)$ and increases monotonically, moving away from the Z -axis.

3.2.3 Summary of Regime 2: The analysis in Regime 2 successfully resolves the dynamics near the degenerate manifold Γ_1 . We find that the unstable node p_0 is preserved at $\mathcal{O}(1)$ coordinates in this scaling. The layer flow pushes trajectories away from this node and onto the attracting critical manifold $\Gamma_5 = \{Z = 0\}$. The reduced problem on Γ_5 is non-trivial at $\mathcal{O}(\tilde{\varepsilon}^2)$ and consists of a slow flow r_2 moving monotonically to the right (increasing U). This flow eventually carries the trajectory out of Regime 2, necessitating a transition to the next regime.

3.3 System X-V (Regime 3): To understand the dynamics near the degenerate manifold Γ_0 of the X-Z system (3.1), we zoom in on Regime 3. We use the coordinate transformation $Z := \varepsilon^2 V$ and the fast time τ_3 defined by the differential relation:

$$(3.13) \quad d\bar{\tau} = \varepsilon^{-2} d\tau_3.$$

With $' = d/d\tau_3$, the original system (3.1) transforms into:

$$(3.14) \quad \left. \begin{aligned} X' &= 2\varepsilon^3 V [\alpha(\sigma_2 X^2 + 1) - \varepsilon^2 X^2 ((\nu - \alpha\sigma_1)V^2 + \nu) + \varepsilon^4 \alpha\sigma_3 V^2] \\ V' &= (1 - \varepsilon^2 \gamma\sigma_1 V) X^2 V^2 - \gamma V (\sigma_2 X^2 + 1) + X^2 - \varepsilon^4 \gamma\sigma_3 V^3 \end{aligned} \right\}$$

We note that this system is in standard form with slow variable X and fast variable V . As in the other regimes, we present this system in the general form of a singularly

perturbed system

$$\begin{aligned}
(3.15) \quad \begin{pmatrix} X' \\ V' \end{pmatrix} &= \underbrace{\begin{pmatrix} 0 \\ 1 \end{pmatrix} (X^2 V^2 + X^2 - \gamma \sigma_2 X^2 V - \gamma V)}_{N_0 f_0(X, V)} + \varepsilon^2 \underbrace{\begin{pmatrix} 0 \\ -\gamma \sigma_1 X^2 V^3 \end{pmatrix}}_{F_2(X, V)} \\
&+ \varepsilon^3 \underbrace{\begin{pmatrix} 2\alpha(\sigma_2 X^2 + 1)V \\ 0 \end{pmatrix}}_{F_3(X, V)} + \varepsilon^4 \begin{pmatrix} 0 \\ -\gamma \sigma_3 V^3 \end{pmatrix} \\
&+ \varepsilon^5 \begin{pmatrix} -2X^2 V ((\nu - \alpha \sigma_1) V^2 + \nu) \\ 0 \end{pmatrix} + \varepsilon^7 \begin{pmatrix} 2\alpha \sigma_3 V^3 \\ 0 \end{pmatrix} \\
&:= N_0 f_0(X, V) + \sum_i \varepsilon^i F_i(X, V), \quad i \in \{2, 3, 4, 5, 7\}.
\end{aligned}$$

to highlight the 6 distinct processes evolving on the timescales $\mathcal{O}(\varepsilon^i)$, $i = 0, 2, 3, 4, 5, 7$.

3.3.1 The layer problem: The layer problem is obtained by taking the limit $\varepsilon \rightarrow 0$:

$$(3.16) \quad \begin{pmatrix} X' \\ V' \end{pmatrix} = \begin{pmatrix} 0 \\ 1 \end{pmatrix} (X^2 V^2 + X^2 - \gamma V - \gamma \sigma_2 X^2 V) = N_0 f_0(X, V).$$

The set of equilibria S_0 , defined by $f_0(X, V) = 0$, forms the critical manifold. By solving for X^2 , we find $X^2 = \gamma V / (V^2 - \gamma \sigma_2 V + 1)$. This defines the one-dimensional folded critical manifold Γ_4 :

$$(3.17) \quad \Gamma_4 = \left\{ \left(\sqrt{\frac{\gamma V}{V^2 - \gamma \sigma_2 V + 1}}, V \right) \mid V \geq 0 \right\}$$

The stability of the critical manifold Γ_4 is determined by the non-trivial eigenvalue $\lambda(X, V) = D_V f_0(X, V) = X^2(2V - \gamma \sigma_2) - \gamma$, which evaluated along Γ_4 , gives:

$$(3.18) \quad \lambda(\Gamma_4) = \frac{\gamma(V^2 - 1)}{V^2 - \gamma \sigma_2 V + 1} \begin{cases} < 0, & V \in \Gamma_{4a} := \{\Gamma_4 : 0 \leq V < 1\} \\ = 0, & V = 1 \\ > 0, & V \in \Gamma_{4r} := \{\Gamma_4 : V > 1\} \end{cases}$$

Thus the critical manifold $\Gamma_4 = \Gamma_{4a} \cup p_4 \cup \Gamma_{4r}$ consists of an attracting branch Γ_{4a} and a repelling branch Γ_{4r} connected at a fold point $p_4 = (\sqrt{\gamma/(2 - \gamma \sigma_2)}, 1)$ where normal hyperbolicity is lost; see Figure 9.

3.3.2 The reduced problem: To obtain the slow flow, we introduce the slow timescale τ_s defined by $d\tau_s = \varepsilon d\tau_3$. This transforms the fast problem (3.15) into the slow problem

$$(3.19) \quad \varepsilon \begin{pmatrix} \dot{X} \\ \dot{V} \end{pmatrix} = N_0 f_0(X, V) + \sum_i \varepsilon^i F_i(X, V), \quad i \in \{2, 3, 4, 5, 7\}$$

where $\dot{\cdot} = d/d\tau_s$. The singular limit $\varepsilon \rightarrow 0$ is only well defined if the phase space is restricted to the critical manifold Γ_4 , i.e., to $f_0(X, V) = 0$.

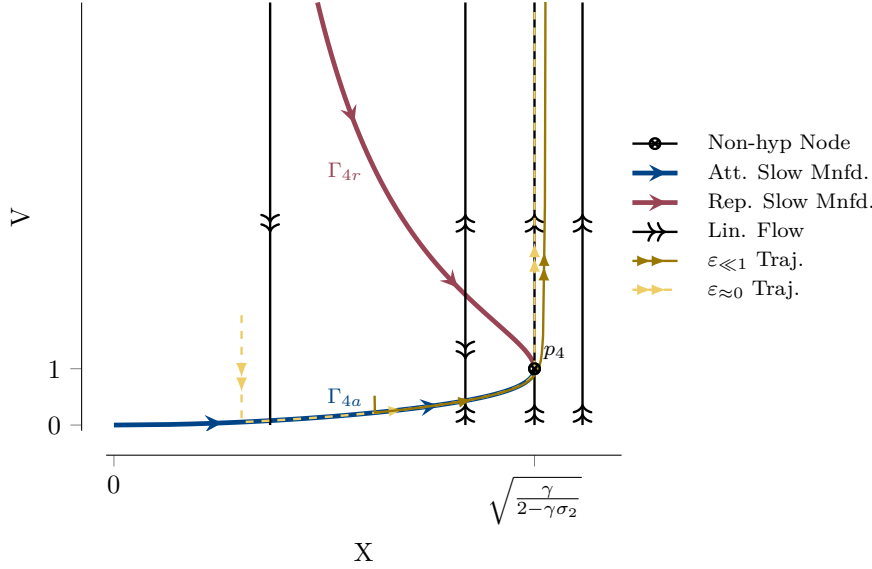


Fig. 9: Analysis of X-V System.

We aim to calculate the slow flow on Γ_4 . Note that the first-order perturbation term F_1 is identically zero. The classical Fenichel approach would next involve projecting the first non-trivial field F_2 onto the tangent space of Γ_4 . This projection is also zero, because the vector field F_2 is vertical, aligning with the fast fibre $N_0 = [0, 1]^T$. The slow (tangent) space is complementary to this fast fibre, and since F_2 has no component in this slow space, its projection vanishes.

This is a degenerate (higher-order) slow flow and, again, we employ the parametrisation method (see section C) to find the leading-order $\mathcal{O}(\varepsilon^3)$ flow. We seek an embedding $\varphi(\xi, \varepsilon)$ and a reduced vector field $r(\xi, \varepsilon)$ satisfying the conjugacy equation (3.11). We use $\xi := V$ as the parameter for the manifold Γ_4 since it is a graph over V ; see (3.17). The expansions are:

$$\begin{aligned}\varphi(\xi, \varepsilon) &= \varphi_0(\xi) + \varepsilon\varphi_1(\xi) + \varepsilon^2\varphi_2(\xi) + \varepsilon^3\varphi_3(\xi) + \dots \\ r(\xi, \varepsilon) &= \varepsilon r_1(\xi) + \varepsilon^2 r_2(\xi) + \varepsilon^3 r_3(\xi) + \dots\end{aligned}$$

with the initial embedding given by the graph $\varphi_0(\xi) = (\varphi_{0,X}(\xi), \xi)^T$, where $\varphi_{0,X}(\xi) = \sqrt{\gamma\xi/(\xi^2 - \gamma\sigma_2\xi + 1)}$.

Solving the hierarchy of infinitesimal conjugacy equations:

- At $\mathcal{O}(\varepsilon)$: Since $F_1 = 0$, we find $r_1 = 0$ and $\varphi_1 = 0$.
- At $\mathcal{O}(\varepsilon^2)$: We solve $J(\Gamma_4)\varphi_2 + F_2(\varphi_0) = \varphi_0' r_2$. Since F_2 is in the direction of the fast fibre N_0 , the projection onto the tangent space gives $r_2 = 0$. However, F_2 yields a non-trivial second-order correction to the manifold embedding:

$$(3.20) \quad \varphi_2(\xi) = \begin{pmatrix} \frac{\gamma\sigma_1\xi^4}{\sqrt{2\xi(\xi^2 - \gamma\sigma_2\xi + 1)^3}} \\ 0 \end{pmatrix}$$

- At $\mathcal{O}(\varepsilon^3)$: We solve $J(\Gamma_4)\varphi_3 + \dots = \varphi_0' r_3 - F_3(\varphi_0)$. This equation involves F_3 (which is non-trivial in the slow direction) and the φ_2 embedding. It yields

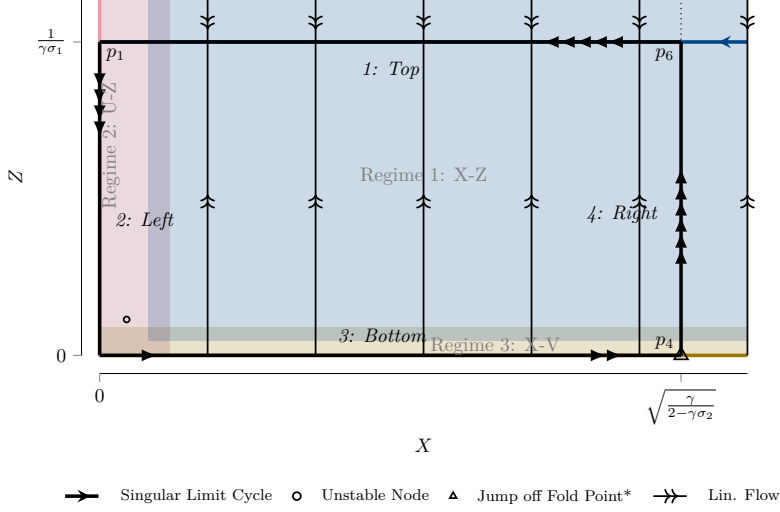


Fig. 10: The Singular Limit Cycle. A composite schematic showing the singular manifolds. The "flow" on the degenerate manifolds Γ_1 and Γ_5 represents the leading-order dynamics revealed by the rescaling analyses in Regimes 2 and 3. The cycle consists of four distinct segments: (1) a slow flow on Γ_2 , (2) a transition from p_1 to the origin (governed by Regime 2), (3) a composite ultra-slow/slow flow on Γ_5 and Γ_{4a} , and (4) a fast jump from p_4 to p_6 .

the first non-trivial reduced vector field r_3 :

$$(3.21) \quad r_3(\xi) = \frac{8\alpha(1+\xi^2)}{1-\xi^2} \sqrt{\frac{\xi^3}{\gamma^3(\xi^2 - \gamma\sigma_2\xi + 1)}} \begin{cases} > 0, & \xi < 1 \text{ (on } \Gamma_{4a}) \\ < 0, & \xi > 1 \text{ (on } \Gamma_{4r}) \end{cases}$$

Thus, the leading-order slow flow, given by $\dot{\xi} = \varepsilon^3 r_3(\xi)$, is directed towards the fold point p_4 (where $\xi = 1$) from both the attracting and repelling branches; see Figure 9.

Remark 3.2. The reduced vector field $r_3(\xi)$ blows up at $\xi = 1$. This pole is the consequence of loss of normal hyperbolicity at p_4 which is a *regular fold (jump) point* (see Definition B.12). It corresponds to a saddle-node bifurcation in the layer problem, and the blow-up of the reduced flow at this point is the characteristic feature.

3.4 Reconstructing the singular limit cycle: Combining the analyses of the different regimes, we can now reconstruct the composite geometry of the singular limit cycle. This reconstruction, shown in Figure 10 (black dashed thick rectangle), is a schematic superposition: it projects the leading-order dynamics revealed by each scaling regime back onto the singular ($\varepsilon = 0$) skeleton. In this limit, the degenerate manifolds Γ_1 and Γ_0 (containing Γ_5) are sets of non-hyperbolic equilibria; the 'flow' we describe on them is the ε -dependent dynamics that emerges upon rescaling. The singular limit cycle, shown in the X-Z coordinates in Figure 10, consists of four distinct segments. We trace the cycle starting from p_6 :

1. *Top segment* ($p_6 \rightarrow p_1$): This segment is the attracting critical manifold Γ_2 from *Regime 1*. The flow is governed by the $\mathcal{O}(\varepsilon)$ reduced problem ($\dot{X} < 0$, (3.5)), moving trajectories slowly towards the Z-axis (p_1).
2. *Left segment* ($p_1 \rightarrow$ origin): This segment is governed by *Regime 2*. The trajectory arrives at p_1 (on the Z-axis, Γ_1) and follows the *Regime 2 layer*

problem ($d/d\tau_2$ time) down the Z -axis. This flow ($Z' < 0$, (3.9)) guides the trajectory to the origin.

3. *Bottom segment* (origin $\rightarrow p_4$): This is a composite segment that begins at the origin:
 - The trajectory first moves along the normally hyperbolic manifold $\Gamma_5 = \{Z = 0\}$ (the X -axis), governed by the *Regime 2 slowest degenerate⁷ reduced problem*. This $\mathcal{O}(\varepsilon^8)$ flow ($r_2 > 0$, (3.12)) carries the trajectory away from the origin.
 - This path is continuous with the attracting branch Γ_{4a} of the folded manifold (from *Regime 3*), which also starts at the origin. As the trajectory moves into the $X \sim \mathcal{O}(1)$ region, its dynamics are characterised by the *Regime 3 degenerate reduced problem*, with a ramped up $\mathcal{O}(\varepsilon^6)$ flow ($r_3 > 0$, (3.21)), which accelerates significantly as it approaches the regular fold point p_4 .
4. *Right segment* ($p_4 \rightarrow p_6$): This is a fast jump. Having reached the fold point p_4 (defined by the *Regime 3* analysis), the trajectory is discharged from the critical manifold. This jump is initially governed by the *Regime 3 layer problem* (see (3.16)) with speed $\mathcal{O}(\varepsilon^2)$, consistent with the *Regime 3 layer timescale* $d\tau_3$. As the trajectory moves away from the degenerate region ($Z \approx 0$) and V becomes large, the flow accelerates further to the $\mathcal{O}(1)$ dynamics of the *Regime 1 layer problem* to complete the connection to the attracting manifold Γ_2 at point p_6 .

We summarise the timescales of the flow on each segment, normalised to the original timescale $\bar{\tau}$, in Table 3.

Table 3: Summary of timescales for each segment of the singular limit cycle, in order of flow.

Segment	Manifold	Analysis	Flow Speed ($d/d\bar{\tau}$)
1. Top	Γ_2	Regime 1 (Reduced)	$\mathcal{O}(\varepsilon)$ (slow)
2. Left	Γ_1	Regime 2 (Layer)	$\mathcal{O}(\varepsilon^2)$ (slower)
3a. Bottom	Γ_5	Regime 2 (Reduced)	$\mathcal{O}(\varepsilon^8)$ (slowest)
3b. Bottom	Γ_{4a}	Regime 3 (Reduced)	$\mathcal{O}(\varepsilon^6)$ (infra-slow)
4a. Right	Layer Flow	Regime 3 (Layer)	$\mathcal{O}(\varepsilon^2)$ (slower)
4b. Right	Layer Flow	Regime 1 (Layer)	$\mathcal{O}(1)$ (fast)

Explanation of timescales: The hierarchy of speeds in Table 3 is derived by normalising all dynamics to the reference timescale $d\bar{\tau}$ of System (2.30).

- $\mathcal{O}(1)$ (*fast*): This is the reference fast timescale of the *Regime 1 layer problem* (3.1). As required by Fenichel theory, the fast jump from p_4 follows these $\mathcal{O}(1)$ dynamics to connect to the attracting manifold Γ_2 at p_6 .
- $\mathcal{O}(\varepsilon)$ (*slow*): This speed arises from the first non-trivial reduced problem in Regime

⁷here, degenerate refers to the dynamics being slower than leading order

1. The flow is driven by the $\mathcal{O}(\varepsilon)$ term in System (3.1) and governs the slow drift along the normally hyperbolic manifold Γ_2 .
- $\mathcal{O}(\varepsilon^2)$ (*slower*): This speed appears in two distinct segments.
 - (a) It governs the *layer dynamics* of Regime 2 (left segment, Γ_1). The local fast time is $d\tau_2 = \varepsilon^2 d\bar{\tau}$ (from (3.6)), so the $\mathcal{O}(1)$ local flow becomes $\mathcal{O}(\varepsilon^2)$ when normalised.
 - (b) It also informs the *layer dynamics* of Regime 3 (right segment), with local fast timescale $d\tau_3 = \varepsilon^2 d\bar{\tau}$ (from (3.13)), resulting in a normalised speed of $\mathcal{O}(\varepsilon^2)$.
 - $\mathcal{O}(\varepsilon^6)$ (*infra-slow*): This speed is captured in the degenerate reduced problem of Regime 3 (bottom segment, Γ_{4a}). The local slow time is $d\tau_s = \varepsilon d\tau_3 = \varepsilon^3 d\bar{\tau}$. In its local timescale, the reduced flow r_3 (3.21) is of order $\mathcal{O}(\varepsilon^3)$, which gives a normalised speed of $\mathcal{O}(\varepsilon^3) \times \varepsilon^3 = \mathcal{O}(\varepsilon^6)$.
 - $\mathcal{O}(\varepsilon^8)$ (*slowest*): This slowest speed is found in the degenerate reduced problem of Regime 2 (bottom segment, Γ_5). The local slow time is $d\tilde{\tau}_s = \tilde{\varepsilon} d\tau_2 = \varepsilon^4 d\bar{\tau}$. The reduced flow r_2 is of order $\mathcal{O}(\tilde{\varepsilon}^2) = \mathcal{O}(\varepsilon^4)$ in this local timescale (from (3.12)). Normalising this gives a speed of $\mathcal{O}(\varepsilon^4) \times \varepsilon^4 = \mathcal{O}(\varepsilon^8)$, explaining the ‘crawl’ away from the origin.

This multi-scale patchwork, comprising various timescale changes across different regimes, is a direct consequence of the singular geometry at the origin, which is rigorously unified using the blow-up method [7, 17, 19, 18, 16, 12].

From Table 3, we can deduce the dynamics of the cycle’s speed. The cycle is dominated by its slow ($\mathcal{O}(\varepsilon), \mathcal{O}(\varepsilon^2)$) and crawling ($\mathcal{O}(\varepsilon^8), \mathcal{O}(\varepsilon^6)$) segments. The cycle is ‘closed’ by a fast jump in the layer flow ($\mathcal{O}(\varepsilon^2), \mathcal{O}(1)$) back to the top. The flow ‘crawls’ away from the origin (speed $\mathcal{O}(\varepsilon^8)$), ramps up to $\mathcal{O}(\varepsilon^6)$, followed by an acceleration along the bottom as it approaches p_4 . It jumps with an initial speed of $\mathcal{O}(\varepsilon^2)$ with significant acceleration to $\mathcal{O}(1)$, relaxes along the top ($\mathcal{O}(\varepsilon)$), and transitions down the Z -axis ($\mathcal{O}(\varepsilon^2)$).

We also point out that our non-dimensionalised model (2.30) is more complicated than the one inherited and analysed in [16] which described a single slow vector field for each regime which invariably yielded a standard slow-fast problem. The mechanistic complexity inherent in the original biophysical model [24, 2, 1] percolates to the dynamics of the non-dimensionalised system, which we have uncovered here.

The above three Regimes 1, 2, and 3 have helped decipher the dynamics at different timescales. The above reconstruction of the singular limit is but an artificial superposition of the regions they define, as shown in Figures 6 and 10, since we have not shown how the different patches connect, including smooth transitions between timescales. To address this *lacuna*, we closely follow the blow-up analysis in [16] to show how the flows transition between timescales.

4 Blow-up analysis: While the scaling analysis revealed the local dynamics within specific regimes, it did not address the global connectivity between them. To prove the existence of a singular limit cycle and establish the geometric ‘gluing’ of these disparate timescales, we employ the blow-up method [17, 18, 16, 7]. This technique desingularises the vector field along the degenerate coordinate axes, unfolding non-hyperbolic critical manifolds onto higher-dimensional spaces where partial hyperbolicity can be recovered. Following the approach in [16], we perform a sequential blow-up to rigorously verify the heteroclinic connections between the flows of Regimes 1, 2, and 3.

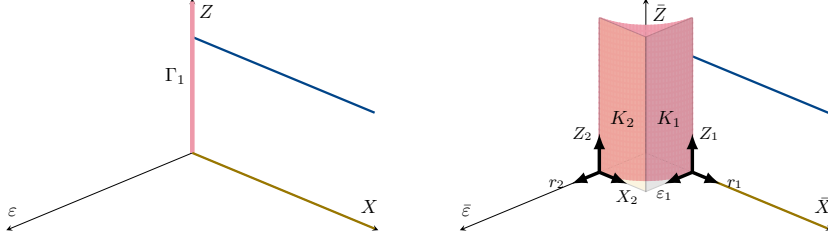


Fig. 11: First Cylindrical Blow-Up

4.1 First cylindrical blow-up: We start by performing a first blow-up of System X-Z (2.30), where the two-dimensional vector field is extended to a three-dimensional system by adding the trivial equation $\varepsilon' = 0$:

$$(4.1) \quad \left. \begin{aligned} X' &= -2\varepsilon Z [(\nu - \alpha\sigma_1)X^2Z^2 - \varepsilon^2\alpha(\sigma_2X^2 + \sigma_3Z^2 + 1) + \varepsilon^4\nu X^2] \\ Z' &= (1 - \gamma\sigma_1Z)X^2Z^2 - \varepsilon^2\gamma Z(\sigma_2X^2 + \sigma_3Z^2 + 1) + \varepsilon^4X^2 \\ \varepsilon' &= 0 \end{aligned} \right\}$$

where $'$ denotes differentiation wrt $\bar{\tau}$. To investigate the degenerate critical manifold branch $\Gamma_1 = \{X = 0\}$, Figure 7, we perform a cylindrical blow-up, as shown in Figure 11, using the transformation:

$$(4.2) \quad X = \bar{r}\bar{X}, \quad Z = \bar{Z}, \quad \varepsilon = \bar{r}\bar{\varepsilon},$$

under the constraint $\bar{X}^2 + \bar{\varepsilon}^2 = 1$. This cylindrical blow-up unfolds the dynamics near Γ_1 by mapping the singular origin to the surface of a cylinder. To analyse the vector field on this manifold, we study the system in a series of overlapping *coordinate charts* that cover the different physical regimes of interest.

4.1.1 Chart K_1 : We define the entry chart K_1 (see Figure 11) by setting $\bar{X} = 1$ and introducing local coordinates $\bar{r} := r_1, \bar{Z} := Z_1, \bar{\varepsilon} := \varepsilon_1$. This yields the transformation $X = r_1, Z = Z_1, \varepsilon = \varepsilon_1 r_1$ and the desingularised system:

$$(4.3) \quad \left. \begin{aligned} r_1' &= -2r_1\varepsilon_1 Z_1 [(\nu - \alpha\sigma_1)Z_1^2 - \varepsilon_1^2\alpha(\sigma_2r_1^2 + \sigma_3Z_1^2 + 1) + \varepsilon_1^4\nu r_1^4] \\ Z_1' &= (1 - \gamma\sigma_1 Z_1)Z_1^2 - \varepsilon_1^2\gamma Z_1(\sigma_2r_1^2 + \sigma_3Z_1^2 + 1) + \varepsilon_1^4r_1^4 \\ \varepsilon_1' &= 2\varepsilon_1^2 Z_1 [(\nu - \alpha\sigma_1)Z_1^2 - \varepsilon_1^2\alpha(\sigma_2r_1^2 + \sigma_3Z_1^2 + 1) + \varepsilon_1^4\nu r_1^4] \end{aligned} \right\}$$

where $'$ denotes differentiation wrt τ_1 given by $d\bar{\tau} = r_1^{-2}d\tau_1$.

Remark 4.1. Chart K_1 covers the transition between Regimes 1 and 2. The transition dynamics are organised by the invariant planes $\varepsilon_1 = 0$ and $r_1 = 0$, which connect at the ‘equator.’⁸

Dynamics in invariant plane $\varepsilon_1 = 0$: Restricting system (4.3) to $\varepsilon_1 = 0$ yields the 2D problem:

$$(4.4) \quad \left. \begin{aligned} r_1' &= 0 \\ Z_1' &= (1 - \gamma\sigma_1 Z_1)Z_1^2 \end{aligned} \right\}$$

⁸Here, the ‘equator’ refers specifically to the two points $\bar{X} = \pm 1$ on the circle $\bar{X}^2 + \bar{\varepsilon}^2 = 1$ (where $\bar{\varepsilon} = 0$), extended along the Z -axis in the blown-up space.

The set of equilibria consists of two lines: $\Gamma_0^D := \{Z_1 = 0\}$ and $\Gamma_2 := \{Z_1 = 1/(\gamma\sigma_1)\}$. Stability is determined by the linearisation of the Z_1 -equation, $\lambda(Z_1) = (2 - 3\gamma\sigma_1 Z_1)Z_1$. Evaluating this along the equilibria shows that Γ_0^D is degenerate ($\lambda = 0$), while Γ_2 is normally hyperbolic and attracting ($\lambda = -1/(\gamma\sigma_1) < 0$). Importantly, we have gained normal hyperbolicity of Γ_2 up to $r_1 = 0$ (point p_1 in Figure 12), which lies on the ‘equator’ of the blown-up cylinder.

Dynamics in invariant plane $r_1 = 0$: Restricting system (4.3) to $r_1 = 0$ yields the 2D problem governing the transition onto the blown-up cylinder:

$$(4.5) \quad \begin{pmatrix} Z_1' \\ \varepsilon_1' \end{pmatrix} = \begin{pmatrix} (1 - \gamma\sigma_1 Z_1)Z_1 - \varepsilon_1^2 \gamma (\sigma_3 Z_1^2 + 1) \\ 2\varepsilon_1^2 [(\nu - \alpha\sigma_1)Z_1^2 - \varepsilon_1^2 \alpha (\sigma_3 Z_1^2 + 1)] \end{pmatrix} Z_1.$$

The set of equilibria comprises the line $\Gamma_0 := \{Z_1 = 0\}$ and two isolated points, p_0 and p_1 , given in (ε_1, Z_1) coordinates by:

$$(4.6) \quad p_0 = \left(\sqrt{\frac{\alpha(\nu - \alpha\sigma_1)}{\sigma_3\alpha^2 + \gamma^2\nu^2}}, \frac{\alpha}{\gamma\nu} \right), \quad p_1 = \left(0, \frac{1}{\gamma\sigma_1} \right).$$

The line Γ_0 (the ε_1 -axis) has a non-trivial eigenvalue $\lambda = -\varepsilon_1^2\alpha \leq 0$. Hence the line Γ_0 is normally attracting for $\varepsilon_1 > 0$ and loses normal hyperbolicity at the origin of the chart, denoted $p_{378} := (0, 0)$.

The first equilibrium p_0 corresponds to the unstable node identified in Regime 2 (see subsection 3.2 for details).

The second equilibrium p_1 corresponds to the intersection of the invariant manifold Γ_2 with the $r_1 = 0$ plane mentioned above. This equilibrium has one stable eigenvalue $\lambda^-(p_1) = -1/(\gamma\sigma_1)$ with eigendirection along the Z_1 -axis and a zero eigenvalue with eigendirection along the ε_1 -axis. The local centre manifold $W_{loc}^c(p_1) \subseteq \Gamma_{12}$ is given to leading order by the quadratic approximation:

$$(4.7) \quad Z_1 = \frac{1}{\gamma\sigma_1} - \frac{\sigma_3 + \gamma^2\sigma_1^2}{\gamma\sigma_1^2} \varepsilon_1^2 + \mathcal{O}(\varepsilon_1^3)$$

The reduced dynamics on this 1D manifold for $\varepsilon_1 \geq 0$ are governed by:

$$(4.8) \quad \varepsilon_1' = \frac{2(\nu - \alpha\sigma_1)}{\gamma^3\sigma_1^3} \varepsilon_1^2 + \mathcal{O}(\varepsilon_1^3)$$

Given $\nu - \alpha\sigma_1 > 0$, the coefficient is positive, indicating that the flow on the manifold is repelling for $\varepsilon_1 > 0$, i.e., moving away from p_1 , which lies on the ‘equator’, onto the cylinder, see Figure 12.

PROPOSITION 4.2 (Existence of the 2D centre manifold). *The 3D system (4.3) possesses a local 2-dimensional centre manifold $W_{loc}^c(p_1)$ at $p_1 = (0, \frac{1}{\gamma\sigma_1}, 0)$, tangent to the (r_1, ε_1) -eigenspace. To leading order, the manifold is represented by the graph:*

$$(4.9) \quad Z_1 = h(r_1, \varepsilon_1) = \frac{1}{\gamma\sigma_1} - \frac{\sigma_3 + \gamma^2\sigma_1^2}{\gamma\sigma_1^2} \varepsilon_1^2 + \mathcal{O}(|(r_1, \varepsilon_1)|^3).$$

The dynamics on $W_{loc}^c(p_1)$ are organised by two invariant 1D sub-manifolds:

mation $X = r_2 X_2, Z = Z_2, \varepsilon = r_2$ and, after desingularisation, the system:

$$(4.10) \quad \left. \begin{aligned} X_2' &= -2Z_2[(\nu - \alpha\sigma_1)X_2^2 Z_2^2 - \alpha(\sigma_3 Z_2^2 + 1) - r_2^2 \alpha \sigma_2 X_2^2 + r_2^4 \nu X_2^2] \\ Z_2' &= (1 - \gamma\sigma_1 Z_2)X_2^2 Z_2^2 - \gamma Z_2(\sigma_3 Z_2^2 + 1) - r_2^2 \gamma \sigma_2 X_2^2 Z_2 + r_2^4 X_2^2 \\ r_2' &= 0 \end{aligned} \right\}$$

where $'$ denotes differentiation with respect to τ_2 ($d\bar{\tau} = r_2^{-2} d\tau_2$). Chart K_2 fully resolves Regime 2, including the Z -axis ($X_2 = 0$) which is inaccessible in Chart K_1 . Notably, in the singular limit $r_2 = 0$, system (4.10) is identical to the System U - Z (3.8), which has already been analysed in subsection 3.2.

The results from the U - Z analysis—specifically the existence of the unstable node p_0 and the attracting critical manifold $\Gamma_5 := \{Z_2 = 0\}$ —directly determine the global fate of the centre manifold $W^c(p_1)$ arriving from the entry chart K_1 . While the local analysis in K_1 shows the trajectory is trapped near the equator, the global topology of the layer problem in K_2 confirms that the flow is repelled by p_0 and subsequently turned by the X_2 -nullcline. This forces a fast heteroclinic connection on the blown-up cylinder from p_1 towards a point p_2 on the critical manifold Γ_5 ; see Figure 8 and Figure 12.

4.1.3 Summary of the First Blow-up: The dynamics following the cylindrical blow-up of $\Gamma_1 = \{X = 0\}$ are obtained by superimposing Charts K_1 and K_2 , effectively desingularising the transition from Regime 1 to Regime 2. Chart K_1 establishes the entry of the flow from the normally hyperbolic attracting manifold Γ_2 . The resulting center manifold $W_{loc}^c(p_1)$ acts as the primary gateway from the macroscopic state space into the singular interior.

As revealed by the global topology in Chart K_1 , the connection from p_1 to p_2 is enforced by a geometric trapping region: the flow is pinched between the tangent line L and the Z_1 -nullcline (blue) locally, while being repelled by the unstable node p_0 globally. This sequence establishes a heteroclinic connection on the blown-up cylinder, mapping the trajectory from the equator onto the critical manifold Γ_5 . Subsequently, the slow flow r_2 on Γ_5 (corresponding to the Regime 2 degenerate reduced problem) carries the trajectory towards the equilibrium p_{378} (see Figure 12), completing the transition across this first degenerate region and setting the stage for the second blow-up.

4.2 Second cylindrical blow-up: To resolve the degenerate dynamics near the non-hyperbolic point $p_{378} = (0, 0)$ in Chart K_1 and describe the transition into the $Z \sim \varepsilon^2$ scaling of Regime 3, we perform a second, weighted cylindrical blow-up. We introduce the transformation:

$$(4.11) \quad r_1 = \hat{r}_1, \quad Z_1 = \hat{s}^2 \hat{Z}_1, \quad \varepsilon_1 = \hat{s} \hat{\varepsilon}_1,$$

subject to the constraint $\hat{Z}_1^2 + \hat{\varepsilon}_1^2 = 1$. This quasi-homogeneous scaling desingularises the vector field at p_{378} , unfolding the singular origin into a cylindrical surface that connects the Regime 2 transition to the Regime 3 exit. The geometry of this second blow-up is presented in Figure 13, and its dynamics are analysed via the transition chart K_3 and the exit chart K_4 .

4.2.1 Chart K_3 : The transition chart K_3 (see Figure 13) is defined by setting $\hat{\varepsilon}_1 = 1$, with local coordinates (r_3, Z_3, s_3) . This yields the quasi-homogeneous trans-

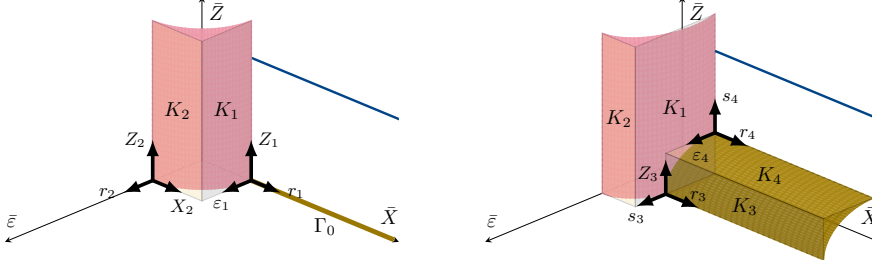


Fig. 13: Second Cylindrical Blow-Up geometry.

formation $r_1 = r_3, Z_1 = s_3^2 Z_3, \varepsilon_1 = s_3$, and the desingularised system:

$$(4.12) \quad \left. \begin{aligned} r_3' &= -2Z_3 r_3 s_3^3 [s_3^2(\nu - \alpha(\sigma_1 + s_3^2 \sigma_3)Z_3^2 + \nu r_3^4) - \alpha(\sigma_2 r_3^2 + 1)] \\ Z_3' &= Z_3^2 + r_3^4 - \gamma(\sigma_2 r_3^2 + 1)Z_3 - s_3^2 \gamma Z_3^3 (\sigma_1 + s_3^2 \sigma_3) \\ &\quad - 4s_3^3 Z_3^2 [s_3^2(\nu - \alpha(\sigma_1 + s_3^2 \sigma_3)Z_3^2 + \nu r_3^4) - \alpha(\sigma_2 r_3^2 + 1)] \\ s_3' &= 2Z_3 s_3^4 [s_3^2(\nu - \alpha(\sigma_1 + s_3^2 \sigma_3)Z_3^2 + \nu r_3^4) - \alpha(\sigma_2 r_3^2 + 1)] \end{aligned} \right\}$$

where $'$ denotes differentiation with respect to τ_3 ($d\bar{\tau} = s_3^{-2} d\tau_3$).

Remark 4.3. Chart K_3 resolves the transition from Regime 2 to Regime 3. The dynamics on the blown-up cylinder are organised by the invariant planes $s_3 = 0$ (the surface of the cylinder) and $r_3 = 0$ (the blown-up Z -axis).

Dynamics in invariant plane $s_3 = 0$: Restricting the system to the invariant plane $s_3 = 0$ yields a 2D flow where r_3 acts as a constant of motion ($r_3' = 0$). The vertical dynamics on the blown-up cylinder are governed by:

$$(4.13) \quad Z_3' = Z_3^2 - \gamma(\sigma_2 r_3^2 + 1)Z_3 + r_3^4.$$

The set of equilibria forms the critical manifold Γ_4 , a parabolic curve in the (r_3, Z_3) plane defined by the roots of the quadratic. This manifold is composed of an attracting branch Γ_{4a} and a repelling branch Γ_{4r} , which meet at the fold point p_4 :

$$(4.14) \quad p_4 = \left(\sqrt{\frac{\gamma}{2 - \gamma\sigma_2}}, \frac{\gamma}{2 - \gamma\sigma_2} \right).$$

At p_4 , the non-trivial eigenvalue $\lambda(r_3, Z_3) = 2Z_3 - \gamma(\sigma_2 r_3^2 + 1)$ vanishes, marking the loss of normal hyperbolicity. Importantly, the attracting branch Γ_{4a} extends to the point p_3 at the origin.

Dynamics in invariant plane $r_3 = 0$: Restricting the system to the invariant plane $r_3 = 0$ reveals the transition from the internal dynamics of the first blow-up to the fold geometry. The 2D flow is given by:

$$(4.15) \quad \begin{pmatrix} Z_3' \\ s_3' \end{pmatrix} = \begin{pmatrix} Z_3^2 - \gamma Z_3 - s_3^2 \gamma Z_3^3 (\sigma_1 + s_3^2 \sigma_3) + 4\alpha s_3^3 Z_3^2 + \dots \\ -2\alpha Z_3 s_3^4 + \mathcal{O}(s_3^6) \end{pmatrix}$$

Factoring Z_3 shows that the set of equilibria comprises the line $\Gamma_5 := \{Z_3 = 0\}$ (the continuation of the attracting manifold from Regime 2) and the isolated point $p_7 = (0, \gamma)$ in the (s_3, Z_3) plane.

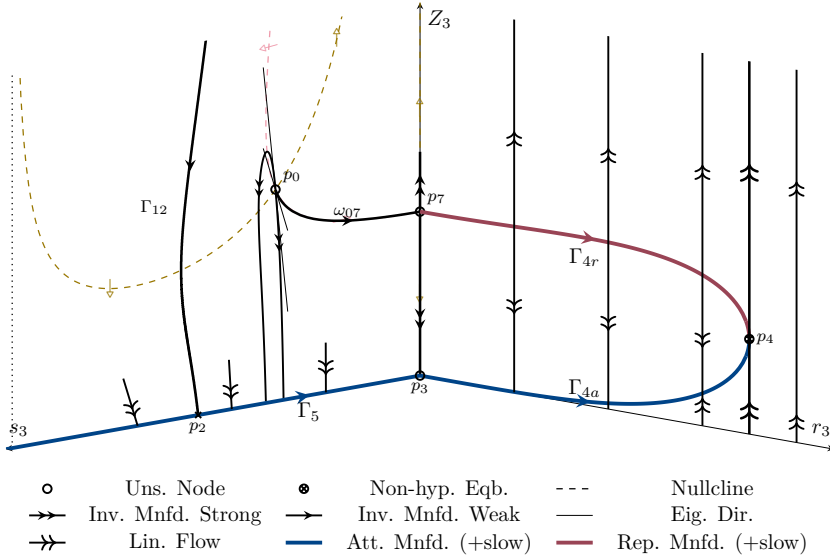


Fig. 14: Chart K_3 with slow-flow overlays.

The point $p_7 = (0, \gamma)$ is a partially hyperbolic equilibrium. Linearisation at p_7 yields $\lambda_1 = \gamma > 0$ in the unstable Z_3 -direction and $\lambda_2 = 0$ in the centre direction s_3 . To leading order, the flow on the corresponding 1D centre manifold is $s'_3 = -2\alpha\gamma s_3^4 + \mathcal{O}(s_3^6)$. For $s_3 > 0$, the centre flow is attracted towards p_7 ($s'_3 < 0$). This configuration establishes a heteroclinic connection from the unstable node p_0 (inherited from Chart K_1 , whose weak unstable manifold on the right connects to the non-hyperbolic point p_{378}) to p_7 . This connection, ω_{07} , serves as a link to the repelling manifold Γ_{4r} .

The manifold Γ_5 is normally hyperbolic and attracting with eigenvalue $\lambda = -\gamma < 0$ up to the point p_3 at the origin, successfully resolving the loss of hyperbolicity at p_{378} in the original coordinates.

The point $p_3 = (0, 0, 0)$ in the full 3D system is a non-isolated equilibrium point representing the corner where the first blow-up scaling ends and the second begins. The Jacobian at p_3 is given by $J(p_3) = \text{diag}(0, -\gamma, 0)$, revealing a stable direction (Z_3) and a 2-dimensional centre subspace in (r_3, s_3) .

PROPOSITION 4.4 (Existence of the 2D centre manifold at p_3). *The 3D system (4.12) possesses a local 2-dimensional centre manifold $W_{loc}^c(p_3)$ at $p_3 = (0, 0, 0)$, tangent to the (r_3, s_3) -eigenspace. To leading order, the manifold is represented by the graph $Z_3 = \Phi(r_3, s_3) = \mathcal{O}(r_3^4)$. The dynamics on $W_{loc}^c(p_3)$ are organised by the two invariant planes that intersect at p_3 :*

- In the invariant plane $r_3 = 0$, the manifold contains the equilibrium branch $\Gamma_5 := \{Z_3 = 0\}$. The flow along Γ_5 is directed towards p_3 .
- In the invariant plane $s_3 = 0$, the manifold contains the attracting branch Γ_{4a} . The flow on this branch is directed away from p_3 .

4.2.2 Chart K_4 : The exit chart K_4 (see Figure 13) is defined by setting $\hat{Z}_1 = 1$ with local coordinates $(r_4, s_4, \varepsilon_4)$, i.e., the transformation $r_1 = r_4, Z_1 = s_4^2, \varepsilon_1 = s_4 \varepsilon_4$

and, after desingularisation, the system:

$$(4.16) \quad \left. \begin{aligned} r'_4 &= -4r_4s_4^3\varepsilon_4 \left[(\nu - \alpha\sigma_1)s_4^2 - \varepsilon_4^2\alpha(\sigma_2r_4^2 + \sigma_3s_4^4 + 1) + \varepsilon_4^4\nu r_4^4s_4^2 \right] \\ s'_4 &= s_4 \left[(1 - \gamma\sigma_1s_4^2) - \varepsilon_4^2\gamma(\sigma_2r_4^2 + \sigma_3s_4^4 + 1) + \varepsilon_4^4r_4^4 \right] \\ \varepsilon'_4 &= -\varepsilon_4 \left[(1 - \gamma\sigma_1s_4^2) - \varepsilon_4^2\gamma(\sigma_2r_4^2 + \sigma_3s_4^4 + 1) + \varepsilon_4^4r_4^4 \right. \\ &\quad \left. - 4s_4^3\varepsilon_4((\nu - \alpha\sigma_1)s_4^2 - \varepsilon_4^2\alpha(\sigma_2r_4^2 + \sigma_3s_4^4 + 1) + \varepsilon_4^4\nu r_4^4s_4^2) \right] \end{aligned} \right\}$$

where $'$ denotes differentiation with respect to τ_4 ($d\bar{\tau} = 2s_4^{-2}d\tau_4$).

Remark 4.5. Chart K_4 resolves the transition from the singular scaling of Regime 3 back to the macroscopic dynamics of Regime 1. The dynamics on the blown-up cylinder are organised by the invariant planes $r_4 = 0$ (blown-up Z-axis), $s_4 = 0$ (surface of the cylinder), and $\varepsilon_4 = 0$ (Regime 1).

Dynamics in invariant plane $r_4 = 0$: Restricting the system to the invariant plane $r_4 = 0$ yields the following 2D flow:

$$(4.17) \quad \begin{pmatrix} s'_4 \\ \varepsilon'_4 \end{pmatrix} = \begin{pmatrix} s_4(1 - \gamma\sigma_1s_4^2 - \varepsilon_4^2\gamma(\sigma_3s_4^4 + 1)) \\ -\varepsilon_4(1 - \gamma\sigma_1s_4^2 - \varepsilon_4^2\gamma(\sigma_3s_4^4 + 1) - 4s_4^5\varepsilon_4(\nu - \alpha\sigma_1) + \dots) \end{pmatrix}$$

The equilibria in this (ε_4, s_4) -plane include the unstable node p_0 , the saddle-node p_1 , and the gateway point $p_7 = (1/\sqrt{\gamma}, 0)$ analysed in the previous chart. The only new equilibrium point introduced in this chart is the origin $p_8 = (0, 0)$.

The origin p_8 is a hyperbolic saddle. The Jacobian at p_8 is diagonal, $J(p_8) = \text{diag}(-1, 1)$, yielding eigenvalues $\lambda_{s_4} = 1$ (unstable) and $\lambda_{\varepsilon_4} = -1$ (stable). This saddle structure acts as a partition, directing trajectories away from the singular scaling and back towards the macroscopic Regime 1 dynamics as s_4 increases.

Remark 4.6 (Resolution of p_{378}). The combination of charts K_3 and K_4 reveals that the loss of normal hyperbolicity associated with the singularity p_{378} is fully resolved. This degenerate point unfolds into a sequence of three desingularised structures: the normally hyperbolic manifold Γ_5 (in K_3), the partially hyperbolic gateway p_7 , and the hyperbolic saddle p_8 (in K_4).

Dynamics in invariant plane $s_4 = 0$: Restricting the system to the invariant plane $s_4 = 0$ (the surface of the cylinder in the exit chart) yields a 2D flow where r_4 is a constant of motion. The vertical dynamics are governed by:

$$(4.18) \quad \varepsilon'_4 = -\varepsilon_4[1 - \varepsilon_4^2\gamma(\sigma_2r_4^2 + 1) + \varepsilon_4^4r_4^4]$$

The set of equilibria includes the normally attracting line $\Gamma_0^S := \{\varepsilon_4 = 0\}$ and the folded critical manifold Γ_4 , defined by the roots of the quadratic in ε_4^2 :

$$(4.19) \quad r_4^4(\varepsilon_4^2)^2 - \gamma(\sigma_2r_4^2 + 1)\varepsilon_4^2 + 1 = 0.$$

This confirms that the manifold Γ_4 identified in Chart K_3 persists in the exit chart. In this representation, p_7 is recovered at $(r_4, \varepsilon_4) = (0, 1/\sqrt{\gamma})$. The fold point p_4 , where the manifold branches meet and normal hyperbolicity is lost, is located at:

$$(4.20) \quad p_4 = \left(\sqrt{\frac{\gamma}{2 - \gamma\sigma_2}}, \sqrt{\frac{2 - \gamma\sigma_2}{\gamma}} \right).$$

The persistence of this parabolic structure across both K_3 and K_4 ensures a continuous transition of the manifold geometry, rigorously establishing the infra-slow crawl

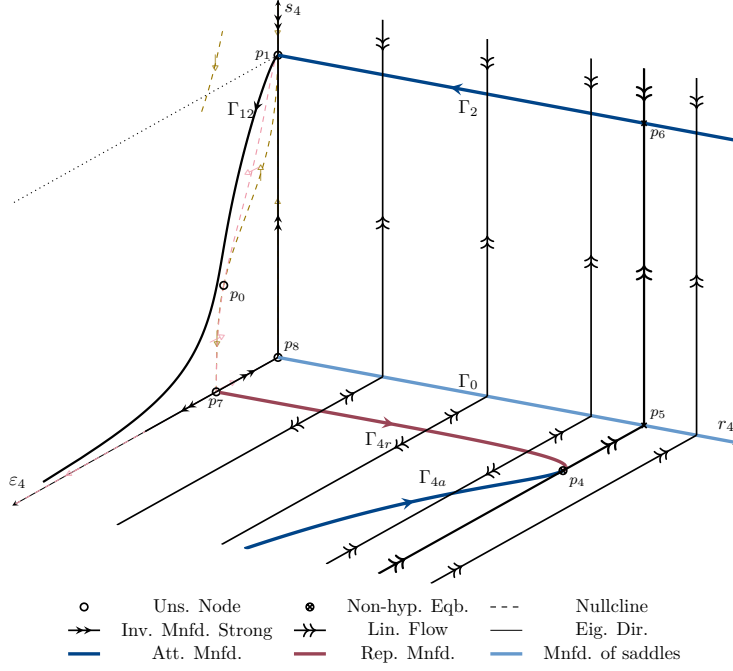


Fig. 15: Chart K_4 with slow-flow overlays.

and subsequent jump that characterises Regime 3.

Dynamics in invariant plane $\varepsilon_4 = 0$: Restricting the system to $\varepsilon_4 = 0$ yields $r'_4 = 0$ and the 1D flow:

$$(4.21) \quad s'_4 = s_4(1 - \gamma\sigma_1 s_4^2).$$

This plane recovers the primary Regime 1 skeleton, serving as the ‘landing zone’ for trajectories exiting the desingularised transition region. The invariant line $s_4 = 0$ captures the local trace of the blown-up repelling critical manifold Γ_{4r} (the X -axis in original coordinates, see Figure 9). More significantly, we recover the stable manifold Γ_2 at $s_4 = 1/\sqrt{\gamma\sigma_1}$.⁹ As illustrated in Figure 15, this recovery establishes the global consistency of the analysis: trajectory segments jumping from the fold point are successfully reinjected into the neighbourhood of the attracting manifold Γ_2 , completing the heteroclinic loop and returning the flow to the macroscopic dynamics of Regime 1.

4.2.3 Summary of the Second Blow-up: The analysis of Charts K_3 and K_4 successfully desingularises the flow through the degenerate point p_{378} , unfolding this singularity into a sequence of hyperbolic and partially hyperbolic structures. The local flow tracking the singular limit cycle within this blow-up is organised as follows:

- *Entry (p_3):* The manifold Γ_5 (accessible in Chart K_3) provides the entry path from Regime 2. The flow along Γ_5 carries trajectories directly into the non-isolated equilibrium p_3 at the origin of the chart.

⁹The square-root relationship between the coordinate $s_4 = 1/\sqrt{\gamma\sigma_1}$ and the K_1 equilibrium $Z_1 = 1/(\gamma\sigma_1)$ is a consequence of the weighted transformation $Z_1 = s_4^2$ used in the second blow-up.

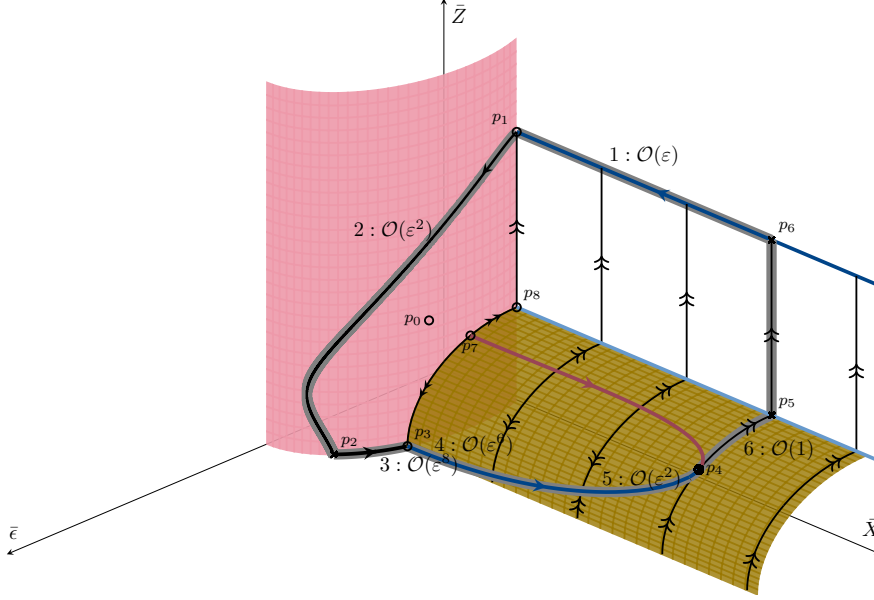


Fig. 16: Singular Limit Cycle. A 3D schematic of the full singular limit cycle in the blown-up space, showing the key points (p_1, p_4, p_6 , etc.) and the path of the trajectory as it moves between the slow manifolds and fast fibers.

- *Manifold Connection ($p_3 \rightarrow p_4$)*: The local centre manifold at p_3 geometrically connects the incoming flow from Γ_5 to the attracting branch of the folded manifold Γ_{4a} . The trajectory moves away from p_3 along Γ_{4a} and accelerates towards the fold point p_4 .
- *Exit Mechanism (Fast Jump)*: Upon reaching the fold point p_4 , normal hyperbolicity is lost. The trajectory is discharged into the fast layer flow. Chart K_4 resolves the topology of this exit, demonstrating how the fast jump escapes the singular scaling past the saddle p_8 , allowing the coordinates to ‘re-inflate’ and connect back to the macroscopic attracting manifold Γ_2 in Regime 1.

This local desingularisation provides the mathematical foundation for the global singular limit cycle to be traced back to the attracting manifold Γ_2 , thereby completing the proof of existence for the periodic orbit.

4.3 The singular limit cycle: The full singular limit cycle Γ^0 is a composite trajectory constructed from the segments analysed in the GSPT ‘patchwork’ and geometrically ‘glued’ together by the blow-up analysis. As illustrated in Figure 16, the cycle is rigorously traced through the sequence of connections $p_1 \rightarrow p_2 \rightarrow p_3 \rightarrow p_4 \rightarrow p_5 \rightarrow p_6 \rightarrow p_1$. This path connects the various critical manifolds and is defined by a distinct hierarchy of timescales that explains the oscillator’s physical phases:

1. *Slow drift ($\mathcal{O}(\epsilon)$)*: Starting at p_6 on Γ_2 , the trajectory moves towards the Z -axis.
2. *Slower deceleration ($\mathcal{O}(\epsilon^2)$)*: At p_1 , the flow is captured by the first blow-up, guiding the trajectory down the Z -axis.
3. *Slowest crawl ($\mathcal{O}(\epsilon^8)$)*: Near the origin, the flow enters the stagnation phase. This represents the long “static” phase of the two-stroke cycle.
4. *Infra-slow acceleration ($\mathcal{O}(\epsilon^6)$)*: Transitioning onto Γ_{4a} , the trajectory begins

to accelerate as it moves along it.

5. *Slower acceleration* ($\mathcal{O}(\varepsilon^2)$): Approaching the fold p_4 , the Regime 3 layer problem dominates, and the trajectory gains significant speed.
6. *Fast jump* ($\mathcal{O}(1)$): At p_4 , the Regime 1 layer problem takes over, causing a near-instantaneous reset back to p_6 .

4.4 Persistence of the periodic orbit We establish that the singular limit cycle Γ^0 persists as a smooth periodic orbit Γ_ε for $0 < \varepsilon \ll 1$. The proof follows from the construction of a Poincaré return map Π_ε on a transverse section Σ . The stability and uniqueness of Γ_ε are guaranteed by the following properties of the transition maps that compose Π_ε :

The singular skeleton Γ^0 contains three normally hyperbolic and attracting slow segments: the macroscopic manifold Γ_2 , the infra-slow manifold Γ_5 , and the ‘accelerating’ manifold Γ_{4a} . By Fenichel theory [8], these segments persist for $\varepsilon > 0$. The corresponding transition maps—specifically those near p_1 and p_3 resolved by centre manifold results, and the passage near p_4 described by the generic fold results of Krupa and Szmolyan [17]—provide cumulative exponential contraction in the Poincaré return map construction. All other components of the cycle involve only algebraic changes in trajectory dispersion and lack any exponential repulsion that could overcome the contraction of the slow manifolds.

As the cumulative exponential contraction dominates the non-exponential transitions, the return map $\Pi_\varepsilon : \Sigma \rightarrow \Sigma$ is a contraction mapping for sufficiently small ε . This implies the existence of a unique, stable, and hyperbolic periodic orbit Γ_ε that converges to Γ^0 in the Hausdorff metric as $\varepsilon \rightarrow 0$, see [6, 10, 20, 30].

5 Conclusion The primary objective of this work was to rigorously analyse the dynamics of the Active Metabolic Oscillator (AMO), the core engine driving pulsatile dynamics in the β -cell Integrated Oscillator Model (IOM). The analysis presented here overcomes three fundamental mathematical hurdles that previously obscured the multiscale nature of this system.

The first challenge was the *non-dimensionalisation* of the original biochemical rate equations. By identifying the relative ratios of maximal enzymatic velocities and substrate affinities, we were able to define a key small parameter, ε , which serves as the ratio of disparate metabolic timescales. This step was essential to recast the AMO as a singular perturbation problem.

Building on this, we addressed the fact that the biophysical model (2.4) is not directly amenable to standard GSPT analysis due to its non-polynomial form and the singularity at $Y = 0$. We applied a state-dependent time rescaling to transform the system into a polynomial ‘surrogate’ relaxation oscillator (2.30). The GSPT and blow-up analyses were thus applied to this surrogate system as a necessary method to resolve the singular geometry that remains hidden in the original model.

The analysis of the surrogate system revealed a vast hierarchy of timescales. Because the time rescaling is state-dependent, these surrogate timescales—stretching from $\mathcal{O}(1)$ to $\mathcal{O}(\varepsilon^8)$ —do not correspond directly to speeds in the biophysical system. However, they provide the essential topological map required to construct a singular limit cycle Γ^0 . Our results show that the two-stroke oscillator is not a simple binary switch, but a multi-layered hierarchy of regimes.

This work significantly extends the analysis of glycolytic oscillators. While our methods were inspired by foundational work on the Goldbeter-Lefever model [16], the distinct biochemical basis of the β -cell AMO (specifically FBP-driven positive feedback) generates a far more intricate singular geometry and a richer timescale

hierarchy than previously studied.

By providing a rigorous way to construct a singular limit cycle where the singular limit was initially inaccessible, this analysis establishes the metabolic subsystem as the master pacemaker for the β -cell's electrical activity. This framework is essential for explaining how the AMO orchestrates complex physiological rhythms, such as compound and accordion bursting, through its intrinsic multi-scale timing mechanism.

Acknowledgments This work was supported by the ARC Discovery Project Grant DP220101817. MW would like to thank Richard Bertram and Patrick Fletcher for the many insightful discussions about the IOM.

REFERENCES

- [1] R. BERTRAM, I. MARINELLI, P. A. FLETCHER, L. S. SATIN, AND A. S. SHERMAN, *Deconstructing the integrated oscillator model for pancreatic β -cells*, *Mathematical Biosciences*, 365 (2023), p. 109085, <https://doi.org/10.1016/j.mbs.2023.109085>.
- [2] R. BERTRAM AND J. E. RUBIN, *Multi-timescale systems and fast-slow analysis*, *Mathematical Biosciences*, 287 (2017), pp. 105–121, <https://doi.org/10.1016/j.mbs.2016.07.003>.
- [3] R. BERTRAM, L. S. SATIN, AND A. S. SHERMAN, *Closing in on the mechanisms of pulsatile insulin secretion*, *Diabetes*, 67 (2018), pp. 351–359, <https://doi.org/10.2337/dbi17-0004>.
- [4] R. BERTRAM, J. TABAK, W. TEKA, T. VO, M. WECHSELBERGER, V. KIRK, AND J. SNEYD, *Mathematical Analysis of Complex Cellular Activity*, vol. 1, Springer International Publishing, 2015, <https://doi.org/10.1007/978-3-319-18114-1>.
- [5] T. R. CHAY AND J. KEIZER, *Minimal model for membrane oscillations in the pancreatic β -cell*, *Biophysical Journal*, 42 (1983), pp. 181–189, [https://doi.org/10.1016/S0006-3495\(83\)84384-7](https://doi.org/10.1016/S0006-3495(83)84384-7).
- [6] C. CHICONE, *Ordinary Differential Equations with Applications*, vol. 34, Springer New York, 2006, <https://doi.org/10.1007/0-387-35794-7>.
- [7] F. DUMORTIER AND R. ROUSSARIE, *Canard cycles and center manifolds*, *Memoirs of the American Mathematical Society*, 121 (1996), pp. 1–100, <https://doi.org/10.1090/memo/0577>.
- [8] N. FENICHEL, *Geometric singular perturbation theory for ordinary differential equations*, *Journal of Differential Equations*, 31 (1979), pp. 53–98, [https://doi.org/10.1016/0022-0396\(79\)90152-9](https://doi.org/10.1016/0022-0396(79)90152-9).
- [9] A. GOLDBETER AND R. LEFEVER, *Dissipative structures for an allosteric model: Application to glycolytic oscillations*, *Biophysical Journal*, 12 (1972), pp. 1302–1315, [https://doi.org/10.1016/S0006-3495\(72\)86164-2](https://doi.org/10.1016/S0006-3495(72)86164-2).
- [10] J. GUCKENHEIMER AND P. HOLMES, *Nonlinear Oscillations, Dynamical Systems, and Bifurcations of Vector Fields*, vol. 42, Springer New York, 1983, <https://doi.org/10.1007/978-1-4612-1140-2>.
- [11] A. L. HODGKIN AND A. F. HUXLEY, *A quantitative description of membrane current and its application to conduction and excitation in nerve*, *The Journal of Physiology*, 117 (1952), pp. 500–544, <https://doi.org/10.1113/jphysiol.1952.sp004764>.
- [12] S. JELBART, K. U. KRISTIANSEN, P. SZMOLYAN, AND M. WECHSELBERGER, *Singularly perturbed oscillators with exponential nonlinearities*, *Journal of Dynamics and Differential Equations*, 34 (2022), pp. 1823–1875, <https://doi.org/10.1007/S10884-021-10041-1/FIGURES/22>.
- [13] S. JELBART, N. PAGES, V. KIRK, J. SNEYD, AND M. WECHSELBERGER, *Process-oriented geometric singular perturbation theory and calcium dynamics*, *SIAM Journal on Applied Dynamical Systems*, 21 (2022), pp. 982–1029, <https://doi.org/10.1137/21M1412402>.
- [14] S. JELBART AND M. WECHSELBERGER, *Two-stroke relaxation oscillators*, *Nonlinearity*, 33 (2020), pp. 2364–2408, <https://doi.org/10.1088/1361-6544/ab6a77>.
- [15] T. J. KAPER, *An introduction to geometric methods and dynamical systems theory for singular perturbation problems*, 1999, <https://doi.org/10.1090/psapm/056/1718893>.
- [16] I. KOSIUK AND P. SZMOLYAN, *Scaling in singular perturbation problems: Blowing up a relaxation oscillator*, *SIAM Journal on Applied Dynamical Systems*, 10 (2011), pp. 1307–1343, <https://doi.org/10.1137/100814470>.
- [17] M. KRUPA AND P. SZMOLYAN, *Extending geometric singular perturbation theory to nonhyperbolic points—fold and canard points in two dimensions*, *SIAM Journal on Mathematical Analysis*, 33 (2001), pp. 286–314, <https://doi.org/10.1137/S0036141099360919>.
- [18] M. KRUPA AND P. SZMOLYAN, *Relaxation oscillation and canard explosion*, *Journal of Differential Equations*, 174 (2001), pp. 312–368, <https://doi.org/10.1006/jdeq.2000.3929>.

- [19] M. KRUPA AND M. WECHSELBERGER, *Local analysis near a folded saddle-node singularity*, Journal of Differential Equations, 248 (2010), pp. 2841–2888, <https://doi.org/10.1016/j.jde.2010.02.006>.
- [20] C. KUEHN, *Multiple Time Scale Dynamics*, vol. 191, Springer International Publishing, 2015, <https://doi.org/10.1007/978-3-319-12316-5>.
- [21] I. LIZARRAGA, B. RINK, AND M. WECHSELBERGER, *Multiple timescales and the parametrisation method in geometric singular perturbation theory*, Nonlinearity, 34 (2021), pp. 4163–4201, <https://doi.org/10.1088/1361-6544/ac04bf>.
- [22] I. LIZARRAGA AND M. WECHSELBERGER, *Computational singular perturbation method for non-standard slow-fast systems*, SIAM Journal on Applied Dynamical Systems, 19 (2020), pp. 994–1028, <https://doi.org/10.1137/19M1242677>.
- [23] I. MARINELLI, P. A. FLETCHER, A. S. SHERMAN, L. S. SATIN, AND R. BERTRAM, *Symbiosis of electrical and metabolic oscillations in pancreatic β -cells*, Frontiers in Physiology, Volume 12 - 2021 (2021), <https://doi.org/10.3389/fphys.2021.781581>.
- [24] I. MARINELLI, T. VO, L. GERARDO-GIORDA, AND R. BERTRAM, *Transitions between bursting modes in the integrated oscillator model for pancreatic β -cells*, Journal of Theoretical Biology, 454 (2018), pp. 310–319, <https://doi.org/10.1016/j.jtbi.2018.06.017>.
- [25] J. P. MCKENNA AND R. BERTRAM, *Fast-slow analysis of the integrated oscillator model for pancreatic β -cells*, Journal of Theoretical Biology, 457 (2018), pp. 152–162, <https://doi.org/10.1016/j.jtbi.2018.08.029>.
- [26] P. SMOLEN, *A model for glycolytic oscillations based on skeletal muscle phosphofructokinase kinetics*, Journal of Theoretical Biology, 174 (1995), pp. 137–148, <https://doi.org/10.1006/JTBI.1995.0087>.
- [27] P. SZMOLYAN AND M. WECHSELBERGER, *Canards in \mathbb{R}^3* , Journal of Differential Equations, 177 (2001), pp. 419–453, <https://doi.org/10.1006/jdeq.2001.4001>.
- [28] T. VO, J. TABAK, R. BERTRAM, AND M. WECHSELBERGER, *A geometric understanding of how fast activating potassium channels promote bursting in pituitary cells*, Journal of Computational Neuroscience, 36 (2014), pp. 259–278, <https://doi.org/10.1007/s10827-013-0470-8>.
- [29] M. WECHSELBERGER, *Geometric Singular Perturbation Theory Beyond the Standard Form*, vol. 6, Springer International Publishing, 2020, <https://doi.org/10.1007/978-3-030-36399-4>.
- [30] S. WIGGINS, *Normally Hyperbolic Invariant Manifolds in Dynamical Systems*, vol. 105, Springer New York, 1994, <https://doi.org/10.1007/978-1-4612-4312-0>.

Appendix A. The IOM and its AMO.

The IOM comprises two interacting oscillatory subsystems: a fast electric one and a slower metabolic one, that are mainly coupled via cytosolic Ca^{2+} ions, and ATP and ADP metabolites.

A.1 Dynamics of the electrical subsystem. The fast electrophysiological subsystem is described by a modified Hodgkin-Huxley formalism, where the membrane potential V and capacitance C are governed by:

$$(A.1) \quad C \frac{dV}{dt} = I_K + I_{KCa} + I_{KATP} + I_{Ca}$$

The calcium current I_{Ca} has a maximal conductance g_{Ca} and reversal (Nernst) potential E_{Ca} . Its gating variable m_∞ is assumed to equilibrate instantaneously with V following a sigmoidal dependence with shape parameters μ_m and σ_m :

$$(A.2) \quad I_{Ca} = g_{Ca} m_\infty(V) (E_{Ca} - V), \quad m_\infty(V) = \frac{1}{1 + \exp((\mu_m - V)/\sigma_m)}.$$

The net transmembrane potassium current consists of three distinct fluxes, all sharing the potassium Nernst potential E_K . The first, I_K , represents delayed rectifying K^+ channels with maximal conductance g_K . Its non-inactivating gating variable n follows first-order kinetics with time constant τ_n and steady-state $n_\infty(V)$ (parameterized by μ_n, σ_n), providing the hyperpolarization necessary to terminate action

potentials:

$$(A.3) \quad I_K = g_K n (E_K - V), \quad \frac{dn}{dt} = \frac{n_\infty(V) - n}{\tau_n}.$$

The second potassium current, I_{KCa} , is essential for burst spiking and is activated by the free cytosolic Ca^{2+} , whose concentration is denoted by Ca_{cyt} . With maximal conductance g_{KCa} and activation function q_∞ , it is given by:

$$(A.4) \quad I_{KCa} = g_{KCa} q_\infty(\text{Ca}_{cyt})(E_K - V), \quad q_\infty(\text{Ca}_{cyt}) = \frac{\text{Ca}_{cyt}^2}{k_d^2 + \text{Ca}_{cyt}^2}.$$

The third current, I_{KATP} , links the electrical and metabolic subsystems. It depends on the cytosolic concentrations of ATP and ADP through the activation function o_∞ . Defining $\text{MgK} = \text{MgADP}/k_{dd}$, the gating is described by:

$$(A.5) \quad o_\infty(\text{ADP}, \text{ATP}) = \frac{0.08 + 0.89\text{MgK}^2 + 0.16\text{MgK}}{(1 + \text{MgK})^2 \left(1 + \frac{\text{ATP}^{4-}}{k_{tt}} + \frac{\text{ADP}^{3-}}{k_{td}}\right)}.$$

A.2 Dynamics of Ca^{2+} ions. The cytosolic Ca^{2+} concentrations are affected by the net fluxes across the cell membrane J_{mem} , the mitochondria [MT] J_{mt} and the endoplasmic reticulum [ER] J_{er} , as shown below, with f_{Ca} as the proportion of free (unbound) Ca^{2+} ions:

$$\frac{d\text{Ca}_{cyt}}{dt} = f_{Ca}(J_{mem} - J_{mt} - J_{er})$$

The net transmembrane flux J_{mem} increases through the influx via the voltage-gated Ca^{2+} ion channels, (A.2), and decreases through the activity of the pump k_{PMCA} .

$$J_{mem} = \frac{\alpha}{V_{cyt}} I_{Ca} - k_{PMCA} \text{Ca}_{cyt}$$

The net flux increases in MT and ER Ca^{2+} are given by

$$\begin{aligned} J_{mt} &= k_{uni} \text{Ca}_{cyt} - k_{NaCa} (\text{Ca}_{mt} - \text{Ca}_{cyt}), \\ J_{er} &= k_{SERCA} \text{Ca}_{cyt} - J_{leak} (\text{Ca}_{er} - \text{Ca}_{cyt}) \end{aligned}$$

The dynamics of free Ca^{2+} within the MT and ER are given respectively by

$$\frac{d\text{Ca}_{mt}}{dt} = f_{Ca} \sigma_{mt} J_{mt}, \quad \frac{d\text{Ca}_{er}}{dt} = f_{Ca} \sigma_{er} J_{er}$$

where σ_{er} and σ_{mt} represent the ratios of cytosolic volume to ER and MT respectively. We refer the readers to [24] for further descriptions of parameters, values and units.

Note that in this IOM model, the transmembrane dynamics governing the exchanges of ADP and ATP between the cytosol and the mitochondria are not modeled, and thus $\text{ADP}_{cyt} = \text{ADP}_{mt} := \text{ADP}$ and $\text{ATP}_{cyt} = \text{ATP}_{mt} := \text{ATP}$. See [23] for an augmented model of the IOM that looks into the latter dynamics.

A.3 Dynamics of the metabolic (glycolytic) oscillator. The biophysical model of the active glycolytic oscillator is described by the following nonlinear dynamical system [24, 1], with state variables F6P and FBP, given in units of μM ,

$$(A.6) \quad \left. \begin{aligned} \frac{dF6P}{dt} &= \frac{1}{1 + K_{GPI}} (J_{GK} - J_{PFK}) \\ \frac{dFBP}{dt} &= \frac{1}{1 + K_{LG}} (J_{PFK} - \frac{1}{2} J_{PDH}) \end{aligned} \right\}$$

Influx of glucose into the cytoplasm triggers the enzyme glucokinase [GK] which leads to the eventual increase of F6P. The latter is consumed with ATP to produce FBP and ADP, which is catalysed by the allosteric enzyme phosphofructokinase [PFK]. FBP positively modulates PFK while cytosolic ATP negatively affects PFK. This substrate depletion mechanism is the basis of the glycolytic oscillations. In the mitochondria, Ca_{mt} positively modulates the activities of the enzyme pyruvate dehydrogenase (PDH) which eventually favours the conversion of ATP to ADP. These are captured by the fluxes J_{GK} , J_{PDH} and J_{PFK} , which are given in units of $\mu M/ms$.

$$(A.7) \quad J_{GK} = \frac{v_{GK}}{1 + (k_{gk}/g_{lce})^{h_{gkglc}}}, \quad J_{PDH} = v_{PDH} \sqrt{\frac{FBP}{1\mu M}}$$

$$(A.8) \quad J_{PFK} = v_{PFK} \frac{(1 - k_{PFK})w_{1110} + k_{PFK} \sum_{i,j,l \in \{0,1\}} w_{ij1l}}{\sum_{i,j,k,l \in \{0,1\}} w_{ijkl}}$$

The weights w_{ijkl} from the Smolen formalism [26], given by

$$(A.9) \quad w_{ijkl} = \frac{(\text{AMP}/K_1)^i (\text{FBP}/K_2)^j (\text{F6P}^2/K_3^2)^k (\text{ATP}^2/K_4^2)^l}{f_{13}^{ik} f_{23}^{jk} f_{41}^{il} f_{42}^{jl} f_{43}^{kl}}$$

depend on the metabolites AMP, ADP and ATP which are assumed to be conserved according to

$$(A.10) \quad \text{ADP} = \frac{\sqrt{\text{ATP}(4A_{tot} - 3\text{ATP})} - \text{ATP}}{2}, \quad \text{AMP} = \frac{\text{ADP}^2}{\text{ATP}}$$

The biophysical parameters and units are given in Table 4.

A.4 Analysis of the dimensionless model. The Jacobian of system (2.4) is given by

$$(A.11) \quad J = \begin{pmatrix} -\hat{\nu}_1 \hat{r}_X & -\hat{\nu}_1 \hat{r}_Y \\ \hat{\nu}_2 \hat{r}_X & \hat{\nu}_2 \hat{r}_Y - \frac{\hat{\gamma}}{2\sqrt{Y}} \end{pmatrix},$$

where the partial derivatives \hat{r}_X and \hat{r}_Y are strictly positive for $X > 0$:

$$\hat{r}_X = \frac{2X(Y + \hat{\sigma}_6)(\hat{\sigma}_3 Y + \hat{\sigma}_4)}{D^2} > 0,$$

$$\hat{r}_Y = \frac{X^2 [(\hat{\sigma}_2 - \hat{\sigma}_1 \hat{\sigma}_6)X^2 + \hat{\sigma}_4 - \hat{\sigma}_3 \hat{\sigma}_6]}{D^2} > 0.$$

Table 4: Parameters for System (A.6)

Par	Val	Unit	Par	Val	Unit	Par	Val	Unit
K_{GPI}	3.33×10^0	1	v_{GK}	1.11×10^{-2}	$\mu M/ms$	K_3	2.24×10^2	μM
K_{LG}	3×10^{-1}	1	v_{PDH}	1.04×10^{-3}	$\mu M/ms$	K_4	3.16×10^1	μM
k_{gk}	1.3×10^1	1	v_{PFK}	1.04×10^{-2}	$\mu M/ms$	f_{13}	2×10^{-2}	1
g_{lce}	7×10^0	1	A_{tot}	3×10^3	μM	f_{23}	2×10^{-1}	1
h_{gkglc}	4×10^0	1	K_1	3×10^1	μM	f_{41}	2×10^1	1
k_{PFK}	6×10^{-2}	1	K_2	1×10^0	μM	f_{42}	2×10^1	1
						f_{43}	2×10^1	1

Table 5: Parameters for biophysical System (2.1)

Par	Val	Unit	Par	Val	Unit	Par	Val	Unit
ω	1.00×10^0	μM	ν	1.04×10^{-2}	$\mu M/ms$	κ_3	3.61×10^{-3}	μM
β	2.31×10^{-1}	1	γ	5.20×10^{-4}	$\mu M/ms$	κ_4	1.89×10^{-4}	1
η	7.69×10^{-1}	1	κ_1	1.12×10^1	$(\mu M)^3$	κ_5	1.55×10^1	$(\mu M)^3$
α	8.61×10^{-4}	$\mu M/ms$	κ_2	8.51×10^0	$(\mu M)^2$	κ_6	1.42×10^2	$(\mu M)^2$

Here, the denominator is $D = \hat{\sigma}_1 X^2 Y + \hat{\sigma}_2 X^2 + \hat{\sigma}_3 Y + \hat{\sigma}_4 > 0$, and the positivity of \hat{r}_Y follows from the parameter constraints $\hat{\sigma}_2 > \hat{\sigma}_1 \hat{\sigma}_6$ and $\hat{\sigma}_4 > \hat{\sigma}_3 \hat{\sigma}_6$. The determinant, trace and discriminant are given by:

$$(A.12) \quad \det(J) = \frac{\hat{\nu}_1 \hat{\gamma} \hat{r}_X}{2\sqrt{Y}} > 0, \quad \text{tr}(J) = -\hat{\nu}_1 \hat{r}_X + \hat{\nu}_2 \hat{r}_Y - \frac{\hat{\gamma}}{2\sqrt{Y}}$$

$$(A.13) \quad \Delta(J) = (\hat{\nu}_1 \hat{r}_X - \hat{\nu}_2 \hat{r}_Y)^2 - \frac{\hat{\gamma}}{\sqrt{Y}} (\hat{\nu}_1 \hat{r}_X + \hat{\nu}_2 \hat{r}_Y) + \frac{\hat{\gamma}^2}{4Y}$$

Evaluated at the equilibrium point (X_{eq}, Y_{eq}) (2.22), with $D_{eq} > 0$, $\hat{r}_X^* > 0$, $\hat{r}_Y^* > 0$ and $X_{eq} > 0$, we have:

$$(A.14) \quad \det = \frac{\hat{\nu}_1 \hat{\gamma} \hat{r}_X^*}{2\sqrt{Y_{eq}}} > 0, \quad \text{tr} = \hat{r}_Y^* - \hat{\nu}_1 \left(\hat{r}_X^* + \frac{\hat{\gamma}^2}{2\hat{\alpha}} \right) > 0$$

$$(A.15) \quad \Delta = (\hat{r}_Y^* - \hat{\nu}_1 \hat{r}_X^*)^2 + \frac{\hat{\nu}_1 \hat{\gamma}^2}{\hat{\alpha}} \left(\frac{\hat{\nu}_1 \hat{\gamma}^2}{4\hat{\alpha}} - (\hat{r}_Y^* + \hat{\nu}_1 \hat{r}_X^*) \right) > 0$$

Based on (A.14) - (A.15), the equilibrium point is an unstable node, which persists in the non-singular limit $\hat{\sigma}_6 > 0$. At the singular limit $\hat{\sigma}_6 = 0$, the equilibrium point $(0, Y_{eq})$ loses hyperbolicity.

Appendix B. Geometric Singular Perturbation Theory (GSPT).

We briefly describe the coordinate-independent setup of GSPT and refer the reader to, e.g., [29] for details. Consider

$$(B.1) \quad x' = F(x; \varepsilon) = F_0(x) + \sum_{i \in \mathbb{N}} \varepsilon^i F_i(x), \quad x \in U_0 \subset \mathbb{R}^n, n \geq 2,$$

where x is the state variable, t is the fast time, $' = d/dt$, and $F(x; \varepsilon)$ is a sufficiently smooth vector field with a power series expansion in the small parameter $0 \leq \varepsilon \ll 1$. The set of singularities of the leading-order vector field $F_0(x)$ is denoted by

$$(B.2) \quad S_0 = \{x \in \mathbb{R}^n : F_0(x) = \mathbb{O}_n\}.$$

DEFINITION B.1. *System (B.1) is called a singular perturbation problem if there exists a subset $S \subseteq S_0$ that forms a k -dimensional differentiable manifold, $1 \leq k < n$. This set S is called the critical manifold.*

Assumption B.2. The leading-order vector field F_0 is a *submersion* on S , i.e., $S = F_0^{-1}(\mathbb{O}_n)$ is locally the zero level set and the Jacobian $DF_0(x)$ has constant rank $n - k$ for all $x \in S$.

B.1 Layer problem and normal hyperbolicity: When System (B.1) is described with respect to the fast timescale t , it is referred to as the *fast system*.

DEFINITION B.3. *The layer problem is the leading-order fast problem in the singular limit $\varepsilon \rightarrow 0$:*

$$(B.3) \quad x' = F_0(x).$$

The critical manifold S consists entirely of equilibrium points for the layer problem.

Assumption B.4. The leading-order vector field can be factored as

$$(B.4) \quad F_0(x) = N_0(x)f_0(x),$$

where $f_0(x) = \mathbb{O}_{n-k}$ defines S as a regular level set. The $n \times (n - k)$ matrix $N_0(x)$ has full column rank for all $x \in S$.

The factorisation in (B.4) naturally induces a *bundle splitting* along S . Specifically, for each $x \in S$, the tangent space splits as:

$$(B.5) \quad T_x \mathbb{R}^n = T_x S \oplus \mathcal{N}_x,$$

where $T_x S = \ker(DF_0)$ is the tangent space to the critical manifold and $\mathcal{N}_x = \text{im}(N_0)$ is the linear fast fiber subspace. The Jacobian of F_0 along S is given by $DF_0|_S = N_0 DF_0$, which has k zero eigenvalues associated with $T_x S$ and $n - k$ eigenvalues associated with \mathcal{N}_x , determined by the matrix $Df_0 N_0|_S$.

DEFINITION B.5. $S_h \subset S$ is *normally hyperbolic* if the matrix $Df_0 N_0|_{S_h}$ is *hyperbolic* (all eigenvalues have non-zero real parts). S_h is *attracting* if all non-trivial eigenvalues have negative real parts.

Normal hyperbolicity ensures that the fast fiber bundle \mathcal{N} is transverse to the tangent bundle TS . This structure is the prerequisite for *Fenichel Theory* [8], guaranteeing that S_h persists as an invariant slow manifold S_ε for $0 < \varepsilon \ll 1$. Where normal hyperbolicity fails, such as at the fold point p_4 , the splitting in (B.5) is no longer transversal as $T_x S \cap \mathcal{N}_x \neq \{0\}$.

B.2 Reduced problem: By rescaling to the slow timescale $\tau := \varepsilon t$, the singular perturbation problem (B.1) is transformed into the *slow system*:

$$(B.6) \quad \dot{x} = \frac{1}{\varepsilon} N_0(x)f_0(x) + F_1(x) + \sum_{i \in \mathbb{N}} \varepsilon^i F_{i+1}(x),$$

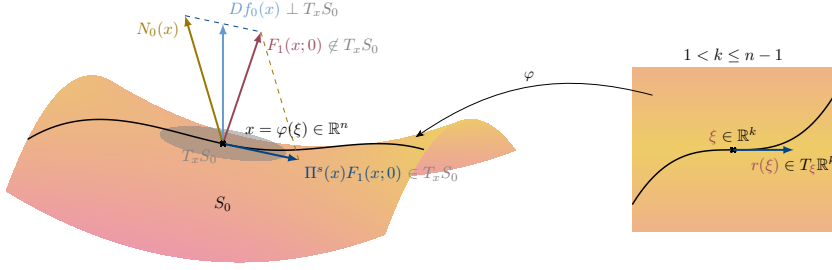


Fig. 17: *Left*: Geometric representation of the reduced vector field obtained via the oblique projection Π^S onto the tangent bundle TS along the linear fast fiber bundle \mathcal{N} . *Right*: Smooth embedding φ from U_1 into U_0 .

where \cdot denotes differentiation with respect to τ . For System (B.6) to be well-defined in the singular limit $\varepsilon \rightarrow 0$, the state space must be restricted to the critical manifold S where $f_0(x) = \mathbb{O}_{n-k}$.

The (leading-order) reduced flow on S is obtained by projecting the first-order vector field $F_1(x)$ onto the tangent space $T_x S$ along the fast fibre bundle \mathcal{N}_x . This requires an oblique projection operator associated with the bundle splitting defined in (B.5).

DEFINITION B.6. *The reduced problem is defined as the limit $\varepsilon \rightarrow 0$ of System (B.6) restricted to S :*

$$(B.7) \quad \dot{x} = \Pi^S(x)F_1(x), \quad x \in S_h,$$

where $\Pi^S(x)$ is the oblique projection parallel to \mathcal{N}_x onto the tangent space $T_x S$.

Remark B.7. The oblique projection onto $T_x S$ is explicitly given by:

$$(B.8) \quad \Pi^S(x) = \mathbb{I}_n - N_0(x) (Df_0(x)N_0(x))^{-1} Df_0(x),$$

with its complementary projection onto the fast fiber subspace, $\Pi^N(x) = \mathbb{I}_n - \Pi^S(x)$; see Figure 17.

B.3 Contact points and loss of normal hyperbolicity: Fenichel theory is applicable only to hyperbolic subsets of the critical manifold. The transition between slow and fast dynamics necessarily occurs through a loss of normal hyperbolicity, which geometrically corresponds to a non-trivial eigenvalue of the layer problem crossing the imaginary axis. We focus on the set of isolated singularities $G \subset S$ associated with the vanishing of a real eigenvalue.

DEFINITION B.8. *The set of contact points $G \subset S$ is defined as:*

$$(B.9) \quad G = \{x \in S : \text{rk}(Df_0(x)N_0(x)) = n - k - 1\}.$$

At these points, the algebraic multiplicity of the zero eigenvalue increases to $k + 1$ while the geometric multiplicity remains fixed at k , implying that the critical manifold S is tangent to the layer flow.

For generic *order-one contact* (contact-folds), the following properties characterize the transition:

LEMMA B.9. *Let G consist of order-one contact points. Then $\det(Df_0(x)N_0(x))$ changes sign upon crossing G along S . Consequently, adjacent normally hyperbolic branches of S meeting at G possess different non-trivial eigenvalue properties.*

DEFINITION B.10 (Adjugate Operator). Let $A \in \mathbb{R}^{m \times m}$ be a square matrix. The adjugate (or classical adjoint) of A , denoted $\text{adj}(A)$, is the transpose of the cofactor matrix of A . For an invertible matrix, it satisfies the relationship:

$$(B.10) \quad \text{adj}(A) = \det(A)A^{-1}.$$

The adjugate provides a smooth extension of the rescaled inverse to singular matrices. Crucially, $\text{adj}(A) \neq \mathbb{O}_{m \times m}$ at a singular point if and only if $\text{rk}(A) = m - 1$.

Remark B.11. The singularity of the projection operator Π^S at G (see Eq. (B.8)) implies that the reduced vector field is ill-defined at contact points. This typically results in a finite-time blow-up of the reduced flow, where the trajectory approaches G with infinite speed in the slow timescale. However, utilizing the smooth extension of the adjugate allows for the evaluation of the desingularized reduced flow direction precisely at the fold.

DEFINITION B.12. A contact point $x \in G$ is called a regular jump point if the following condition holds:

$$(B.11) \quad N_0(x) \text{adj}(Df_0(x)N_0(x)) Df_0(x)F_1(x) \neq \mathbb{O}_n.$$

At a regular jump point, the reduced flow is aligned with the non-trivial kernel of the layer Jacobian. This alignment defines the locus and direction where the system switches from slow dynamics to the fast fibers of the layer problem. Note that the condition in Definition B.12 is only non-trivial for order-one contact points ($n - k - 1$); if the rank were to drop by two or more, the adjugate would vanish identically. In the context of the AMO model, the point p_4 represents such a regular fold where the trajectory is ejected towards the fast reset phase.

Appendix C. Parametrisation method.

To evaluate the reduced vector fields on higher-order slow manifolds, we use the *parametrisation method*, whose summary here closely follows the treatment in [21].

We adopt the exact setup and notation from section B for the singularly perturbed system (B.1), including the factorisation $F_0 = N_0 f_0$, the transverse bundle splitting, and the oblique projection operators Π^S and Π^N . Recall that if the critical manifold S is normally hyperbolic, Fenichel theory [8] guarantees the existence of a nearby invariant slow manifold S^ε for $0 < \varepsilon \ll 1$. To employ the parametrisation method, we require an explicit representation of this base manifold:

Assumption C.1. The k -dimensional normally hyperbolic critical manifold S ($1 \leq k \leq n - 1$) is the image of a smooth embedding

$$(C.1) \quad \varphi_0: U_1 \subset \mathbb{R}^k \hookrightarrow U_0 \subset \mathbb{R}^n.$$

C.1 Embedding and reduced vector field: To find the slow flow on the perturbed manifold S^ε , we search for a smooth embedding φ and a reduced vector field r with the following asymptotic expansions:

$$\begin{aligned} \varphi: U_1 \times [0, \varepsilon_0] &\hookrightarrow U_0, & \varphi(\xi; \varepsilon) &= \varphi_0(\xi) + \sum_{i \in \mathbb{N}} \varepsilon^i \varphi_i(\xi) \\ r: U_1 \times [0, \varepsilon_0] &\rightarrow \mathbb{R}^k, & r(\xi; \varepsilon) &= \sum_{i \in \mathbb{N}} \varepsilon^i r_i(\xi), & \xi' &= r(\xi; \varepsilon) \end{aligned}$$

where $x(t) := \varphi(\xi(t); \varepsilon)$ satisfies $x' = F(x; \varepsilon)$ whenever $\xi' = r(\xi; \varepsilon)$. The pair (φ, r) satisfies the *conjugacy equation*:

$$(C.2) \quad \mathcal{F}(\varphi, r)(\xi, \varepsilon) = D_\xi \varphi(\xi, \varepsilon) \circ r(\xi; \varepsilon) - F(\varphi(\xi, \varepsilon), \varepsilon) = 0.$$

C.2 Iterative algorithm for solving the conjugacy equation: Matching the powers of ε following a Taylor expansion of (C.2) leads to a hierarchy of infinitesimal conjugacy equations. Utilizing the factorisation $F_0 = N_0 f_0$ and the fact that $D_x F_0|_S = N_0 D_x f_0$, the equation for the j -th order unknown pair (φ_j, r_j) is:

$$(C.3) \quad D_\xi \varphi_0 \circ r_j - N_0(\varphi_0) D_x f_0(\varphi_0) \circ \varphi_j = G_j,$$

where G_j depends only on the previously determined terms $\{\varphi_i, r_i\}_{i < j}$. Given the splitting $D_\xi \varphi_0 \circ r_j \in T_x S$ and $N_0 D_x f_0 \circ \varphi_j \in \mathcal{N}_x$, the update formulas are obtained by applying the projection operators Π^S and Π^N :

- *Reduced slow dynamics update (r_j):* Applying Π^S eliminates the fiber component of the homological error. Since $\Pi^S G_j$ lies in the tangent space $T_x S = \text{im}(D_\xi \varphi_0)$, and φ_0 is an immersion, there exists a left inverse $(D_\xi \varphi_0)^L$ such that $(D_\xi \varphi_0)^L D_\xi \varphi_0 = \mathbb{I}_k$. This yields the internal dynamics update:

$$(C.4) \quad r_j(\xi) = (D_\xi \varphi_0)^L [\Pi^S(\varphi_0(\xi)) G_j(\xi)].$$

- *Slow manifold update (φ_j):* Applying Π^N isolates the fiber component. Normal hyperbolicity ensures that the ‘restricted’ Jacobian $D_x f_0 N_0$ is invertible. The correction to the manifold embedding is given by:

$$(C.5) \quad \varphi_j(\xi) = -(D_x f_0)^R (D_x f_0 N_0)^{-1} D_x f_0 G_j(\xi),$$

where $(D_x f_0)^R$ is a right inverse of $D_x f_0$, i.e., $D_x f_0 (D_x f_0)^R = \mathbb{I}_{n-k}$.

Remark C.2. The updates r_j and φ_j are subject to choices of the generalised inverses $(D_\xi \varphi_0)^L$ and $(D_x f_0)^R$. These choices allow one to preserve specific structural properties of the manifold:

- The choice of $(D_\xi \varphi_0)^L$ in (C.4) determines how the tangential error is mapped into the internal coordinates ξ . While the Moore-Penrose pseudoinverse provides an ‘optimal’ least-squares orthogonal projection, it may not respect the chosen parametrisation. In a *graph parametrisation*, $(D_\xi \varphi_0)^L$ is typically chosen to ensure the manifold remains a graph over the base variables ξ by extracting only the components corresponding to the base space.
- Similarly, the choice of $(D_x f_0)^R$ in (C.5) determines the direction of manifold deformation to correct the normal error. While the GSPT-natural choice is the *oblique, fiber-aligned* update $(D_x f_0)^R = N_0 (D_x f_0 N_0)^{-1}$, which shifts S strictly along the dynamical fast fibers \mathcal{N}_x , one might instead choose $(D_x f_0)^R$ to lie in the *orthogonal complement* of the tangent space (geometric fibers) to preserve a specific coordinate-based graph structure.

Any tangential component introduced by these choices corresponds to a reparametrisation of the manifold and is compensated by a corresponding shift in the reduced vector field r_j to satisfy the conjugacy equation.